

TABLE OF CONTENTS

	Page
Chapter 1: Introduction	1
1.1 Motivations for study of WDM	4
1.2 Experimental Generation of WDM	7
1.3 X-ray diagnostics of WDM	10
1.4 Dissertation Outline	19
Chapter 2: Physics of PENELOPE	20
2.1 Types of interactions	20
2.2 Inelastic scattering	26
2.3 Accuracy and useful regimes	30
2.4 Inelastic scattering	33
2.5 Dosimetry	34
Chapter 3: A Photometric Study of Energy-Dispersive X-ray Diffraction at a Laser Plasma Facility	36
3.1 I Introduction	36
3.2 II Methods	40
3.3 III Results and discussion	49
3.4 IV. Conclusions	59
3.5 Acknowledgements	59
3.6 References	61
Chapter 4: X-ray Free Electron Laser-Based Studies of WDM	62
4.1 X-ray Free Electron Lasers	62
4.2 HED physics at XFEL facilities	65
4.3 Scientific Directions	66
4.4 Design of an XFEL heating experiment	67
4.5 Experimental Work	68

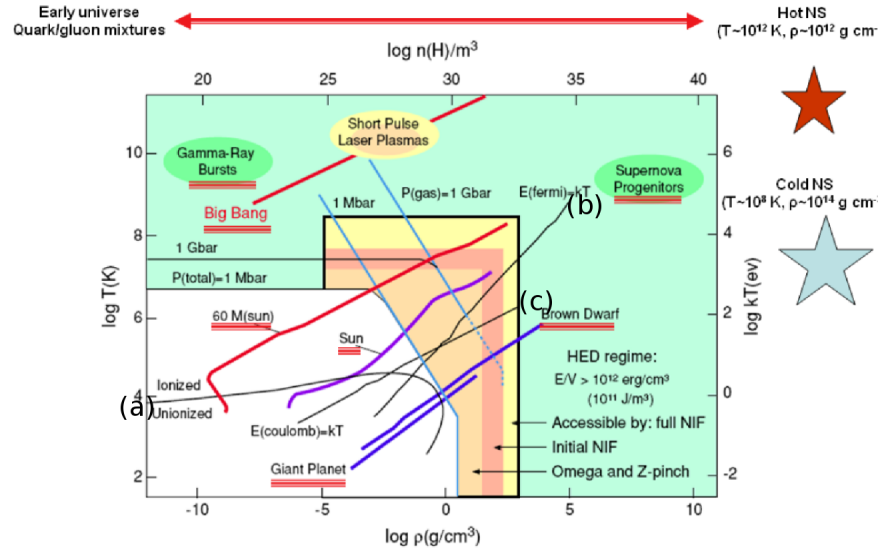
Chapter 1

INTRODUCTION

In this thesis I introduce the development of new techniques for the production of materials in the warm dense matter (WDM) regime, and for interrogation of the structure and thermodynamic state of such systems using x-ray diffraction and (to a lesser extent) spectroscopy. The main results include a scheme for single-shot determination of the static structure factors of WDM systems generated at laser plasma facilities; a technique for enhancing the density of deposited energy in WDM generated at fourth-generation X-ray sources such as the Linac Coherent Light Source (LCLS); and interpretation of experimental data that puts new constraints on the thermalization (both electronic and lattice) of a solid state material upon fs-scale XFEL heating. In addition to this thread of research I discuss some secondary work on the development of software and electronics for energy- and position-sensitive pixel detectors including current applications in the context of soft x-ray laboratory and possible future ones in XFEL, synchrotron, and laser plasma facility-based experiments.

Before proceeding it is useful to define WDM in terms of the microphysical context it occupies. Fig. (which figure) presents a map of thermodynamic parameter space, with the logarithm of density and temperature on the horizontal and vertical axes, respectively. A few bounding curves can be identified. First, ionization occurs at temperatures exceeding approximately 1 eV; this is denoted by curve (a), which forms a boundary between the plasma and condensed matter regimes. Second, curve (b) indicates the boundary at which the Fermi energy is approximately equal to the average thermal energy $k_B T$; i.e. where the electron degeneracy parameter, $E_f/k_B T$ is of order unity. Third, curve (c) corresponds to a value of 1 for the ratio of the Coulomb energy to the thermal to the thermal one, also called the plasma coupling parameter Γ .

Figure 1.1: The atlas of high-energy density physics (cite)



Above curves (a), (b) and (c) is the regime of classical plasma physics where, as a result of the weak interaction between neighboring ions ($\Gamma \ll 1$), collective interactions predominate over binary collisions and quantum statistics can be neglected ($\Lambda \ll 1$) except for the purpose of calculating blackbody spectra. In this regime continuous, classical modeling treatments are widely-used and fully validated (cites). Below curves (a), (b), and (c) is the low-temperature, intermediate-density realm of condensed matter physics, where the established theoretical framework is that of many-body quantum mechanics, wherein the potential landscape is built on the interaction between electrons and ion cores. In this framework finite-temperature effects are incorporated perturbatively. WDM occupies the transitional regime above curve (a) and near the intersection of curves (b) and (c), characterized by partial degeneracy and strong ion-ion coupling (Γ and Λ of order unity). As a result, treatments of plasma physics originating in the classical regime are not applicable to WDM. Solid state physics models similarly fail in the WDM regime due to large, non-perturbative effects of finite temperature on the structure and thermodynamics of WDM (cites).

Modeling of the ionization potential depression (IPD) in a plasma is a case in point of the difficulties that manifest themselves with theoretical treatments of WDM. Adequate descriptions of IPD are given the Debye-Hueckel approximation and ion sphere model, which cover opposite regimes of high temperature and low density, and low density and high temperature, respectively. We here briefly introduce both model, with focus on the assumptions and approximations that they adopt.

The Debye-Hueckel model applies to a weakly-coupled plasma in local thermal equilibrium. It identifies the electrostatic potential in the Poisson equation with the mean field generated by a population of Maxwell-Boltzmann-distributed ions or electrolytes. This results in the Poisson-Boltzmann equation which, when solved, gives the electrostatic potential produced by an arbitrary charge distribution. The condition for validity of the Debye-Hueckel model is for the Thomas-Fermi screening length (also called the Debye length) to be much larger than the mean inter-ion separation. This condition is satisfied at comparable temperatures, but lower densities, than those encompassed by the WDM regime. (check that this is right, and cite)

In the opposite limit, the ion-sphere model describes IPD in a high-density material with $\Gamma > 1$ (in the low-temperature context IPD is more commonly referred to as pressure ionization). The picture offered by the ion-sphere model is that of a plasma with highly-correlated ion positions and therefore no close encounters between ion pairs. Each ion is treated as a sphere whose potential is unaffected by the presence of neighboring ions. (cite Stewart-Pyatt). The sphere radius is $R_0 = (3/4\pi N_i)^{1/3}$, where N_i is ion number density, while the orbital radius of the ion sphere's n th principal energy level is approximately $r_n = (n^2/Z_n)(0.529\text{\AA})$. For the n th bound state to exist it is necessary that $r_n \leq R_0$; thus, IPD manifests itself as a reduction in the number of bound states as a function of the inter-ion distance R_0 . It should be noted that, although the ion-sphere model is a frequently-used heuristic in high-temperature plasmas with near-ambient densities, it is known to be incorrect in the high-density, moderate-temperature ($\Gamma \gg 1$) regime. Neaton et al. have done ab-initio (DFT) simulation of Li—a free electron-like material under ambient conditions—showing

that, contrary to intuitive expectations and the ion-sphere model, it becomes less free-electron like at high densities and additionally loses its common bcc crystal structure. (cite Neaton 1999) Due to overlap of core electrons, the treatment of electronic wavefunctions in this regime is necessarily strongly nonperturbative—again in conflict with the ion-sphere model’s assumptions.

Leaving aside, momentarily, the ion sphere model’s limitations, we might contemplate constructing a model of ionization potential depression that reduces to the ion sphere and Debye-Huekel models in their respective limits. Doing so is challenging because it allows none of the simplifying approximations invoked by the two limiting cases. One manifestation of uncertainty of the correct approach is the existence of two mutually-contradictory models for IPD in WDM, those of Stewart and Pyatt (cite) and Ecker and Kroll (cite). Though the Stewart-Pyatt model is more widely used and has the virtue of reproducing the ion-sphere and Debye-Hueckel behaviors (cite Crowley review article), its validity has been called into question by recent direct XFEL-measurements of IPD in Al heated to 180 eV (cite Cricosta paper). Such conflicts exemplify the persistent difficulty of constructing models with validity accross different sub-regimes of WDM.

1.1 Motivations for study of WDM

In addition to the basic physics questions intrinsic to the WDM regime, there are a number of points of contact between WDM and particular problems in other fields. This interaction has been bolstered in recent years by rapid development of laser plasma facilities and x-ray free electron lasers (XFELs) with unprecedeted experimental capability for producing WDM and probing its physical properties. This has brought many previously-intractable physical regimes into the scope of both empirical investigation and numerical simulation.

1.1.1 Astrophysical modeling

A large contribution to this growth in interest is the relevance of WDM theory as a microphysical basis on for models of various systems in planetary and stellar astrophysics. Here

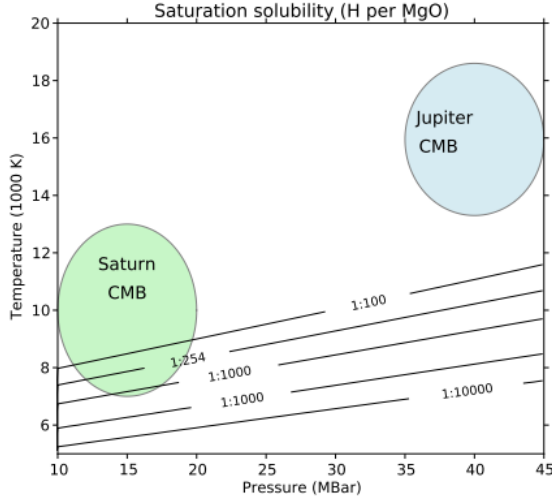
we introduce two examples in which this relationship is salient.

The interiors of both rocky and gas giant planets contain dense, and in some cases Fermi-degenerate, plasmas at 1 eV-scale temperatures. Examples include the iron under conditions of the earth's core (pressure = 3 Mbar; T = 6000 K), whose viscosity and equation of state (EOS) has consequences on convective heat transfer and the formation of earth's magnetic field. (cites) Similarly, modeling of the evolution and structure of gas giant planets depends on the EOS of H under the regime of gas giant interiors. The existence of metallic H caused by pressure ionization at Mbar-scale pressures has been experimentally demonstrated, but its onset is poorly understood at the level of theoretical models for the EOS: although a first-order dielectric-to-metal phase transition has been postulated, current approaches do not attempt to model pressure ionization, instead limiting themselves to interpolation between the better-understood atomic and fully ionized limits. (cites)

The solubility physics of two-component WDM mixtures containing H with other species found in rocky planetary bodies has direct consequences on mass transport across the core-mantle boundary in gas giant planets. It also has crucial importance in the modeling of gas giant formation, where the solubility of H with rocky elements bears on the plausibility of the planetesimal accretion hypothesis for gas giant genesis, which requires condensation of H and He around a rocky core. (cite Wilson MgO solubility paper).

Another case in which the material properties of warm dense matter determine the behavior of an astrophysical object is that of white dwarves, whose envelopes consist of a hot, partially Fermi-degenerate plasma. Modeling the cooling of white dwarves is a topic of interest (cites), especially in the context of the importance of type 1a supernovae as ‘standard candles’ for measuring distances to distant galaxies. Doing so, however, requires knowledge of stellar envelope opacities, equations of state (EOS), and transport properties, many of which properties are currently unknown to within factors of order unity. The absence of understanding of the simplest available system—the hydrogenic one-component plasma—underscores the difficulty of this thread of research.

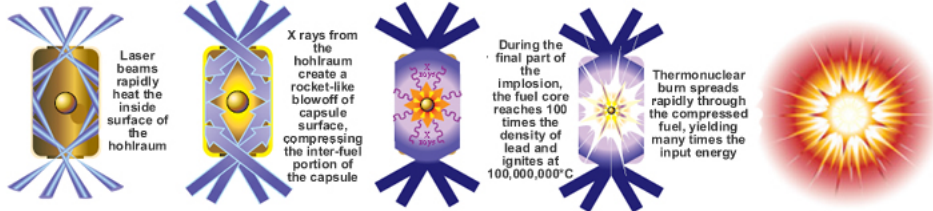
Figure 1.2: Saturation solubility of MgO in H as a function of pressure and temperature from *ab initio* calculation by Wilson et al. The temperature conditions of the core-mantle boundaries of Saturn and Jupiter are indicated. (cite Wilson)



1.1.2 Inertial Confinement Fusion

The effort to reach controlled fusion through implosion of deuterium-tritium fuel capsules—an approach termed inertial confinement fusion—has progressed significantly in the last decade due to completion of laboratory facilities capable of producing HED (definition?) plasmas with densities and temperatures approaching levels needed for ignition. Fig. (which figure) shows a schematic of an ignition technique called indirect drive. In this configuration the ICF target, which consists of a hollow spherical capsule of ablator material filled with deuterium-tritium fuel, is confined in a hollow capsule of a high-Z material (the Hohlraum). A multi-TW, ns-duration duration laser passes through apertures in the Hohlraum and heats the Hohlraum to blackbody temperatures on the order of several hundred eV. The resulting thermal spectrum of soft X rays isotropically heats and ablates the fuel capsule's surface, causing its interior to implode by conservation of momentum. Typical parameters of the plasma created at maximum compression include areal densities (capsule density \times radius) of 0.3 g/cm² and temperatures of the order 10 keV. (cite. see x-games pg 113)

Figure 1.3: Schematic of indirect-drive inertial confinement fusion shot. (cite)



Although its end state falls well within the regime of a classical plasma, the fuel capsule transitions through the WDM state during compression. The opacity and EOS of warm dense matter therefore has a strong influence on the development and propagation of shocks during ablation of the fuel capsule, which in turn affects the optimization of various experimental parameters, including fuel capsule geometry and temporal profile of the laser driver. Accurate modeling of the fuel capsule's transport properties under the WDM regime is equally important for understanding the development during compression of hydrodynamic instabilities, which are known to be a major obstacle to the efficient coupling of laser energy into fuel compression (cites).

1.2 Experimental Generation of WDM

WDM conditions may be generated using X-ray free electron lasers (XFELs) and several varieties of lasers, found both in large-scale facilities and laboratory-scale systems. Here we provide an overview of existing technologies.

1.2.1 Long-pulse lasers

Lasers with pulse durations on the order of nanoseconds and energies of 1 kJ or more are among the most versatile tools for producing high energy density states, including warm dense matter. In the most common use cases of long pulse lasers the target is a bulk material, and coupling of laser energy into it occurs in two stages. First, the laser rapidly (TODO how rapidly) generates a coronal plasma at the material's surface. Once the electron

density of this plasma exceeds the laser wavelength's critical density (TODO: equation) the laser becomes electromagnetically shielded from the material's interior and can no longer transfer energy to it. In the context of direct drive (where the material is a target to which laser energy is directly coupled), subsequent energy transfer occurs by thermal conduction of energy from the surface plasma to higher-density regions as well as by compression of the target resulting from ablation of its surface. In the case of indirect drive, the laser's energy is used to heat a surface (typically the interior of a Hohlraum) that provides a thermal bath which, in turn, couples to the target via its blackbody radiation.

The ns duration of long-pulse lasers matches the timescale on which mechanical and hydrodynamic processes occur on typical target scales. Long-pulse lasers are thus suited to generating ramp and shock compression, notably including for the application of ICF. The largest-scale laser plasma facilities—Omega EP at the Laboratory for Laser Energetics in Rochester, NY and the National Ignition Facility—are long-pulse laser systems targeted toward the ICF program.

1.2.2 Short-pulse lasers

Short pulse lasers are a second class of systems used to generate HED conditions. They are typically defined by pulse durations on the order of a picosecond or less, down to as little as ~ 1 fs.

Short-pulse laser systems arose after the development of chirped pulse amplification in the 1980s (cite) and have proliferated ever since (cites), especially with the recent advent of compact (university laboratory-scale) versions with tens of Joules of pulse energy, sufficient to generate scientifically interesting HED conditions. The largest-scale short pulse lasers have pulse powers up to 100 TW (check this number), with durations between 10 and 100 fs (check this as well).

Due to the smaller total energies of short-pulse lasers and the relatively slow cooling timescale of materials heated above ambient conditions *regardless* of the pump duration, short-pulse lasers are used to generate HED conditions under direct-drive configurations

alone. Energy is coupled into a target indirectly (as is the case with long-pulse systems) via ‘hot’ MeV-scale electrons generated in the laser’s interaction with plasma at the target surface. In the (typical) case where bulk heating is required, the target thickness is small compared to the hot electrons’ stopping range, causing them to reflux through the target once it acquires net positive charge. This process lasts on the order of one ps (check this, cite Nilson and maybe others) and thus sets the time resolution of experiments in which the short-pulse laser is used to both heat and probe the target.

1.2.3 X-Ray Free Electron Lasers

The advent of X-Ray Free Electron lasers is a major advance in capability for WDM research. Existing incarnations of these sources, notably the Linac Coherent Light Source (LCLS), provide 10^{14} photons in a ≥ 10 fs-duration monochromatic pulses with tunable energy. While the energies per pulse are smaller than those attainable with a short-pulse laser, they are largely sufficient to produce HED states with temperatures in excess of 100 eV (cite). Because XFELs can heat volumetrically, they are free of the primary deficiency of lasers with respect to the task of generating dense plasmas: namely, the latter can only heat bulk materials indirectly and over durations of 1 ps or longer, which exceeds the timescale for changes in WDM, preventing the study of short-lived transient states.

The ability to generate (and probe) WDM on truly inertial timescales, wherein atomic nuclei are effectively frozen, has been duly exploited in early pioneering studies at the LCLS. It forms the basis, for example, for a new thread of materials science research on nonthermal lattice and spin dynamics (cite Lee and others). Likely even more significantly, it is the enabling feature for macromolecular crystallography under the ‘diffract before destroy’ paradigm. (cites) The possibilities surrounding rapid generation of WDM is a topic to which I return in (which chapter?). (cite Vinko et al. and other early LCLS papers).

1.3 X-ray diagnostics of WDM

Experimental studies of WDM suffer from a substantial complication: the opacity of WDM to photons is large at energies up to the soft X ray regime. As mentioned in section 1.2.2, in the context of laser heating this is merely a frustration; for the purposes of measuring the conditions of a bulk WDM system, however, the need for direct detection of radiation originating from the target's interior makes optical probes wholly ineffective. Determination of the structure and thermodynamic state variables of a dense plasma therefore requires sufficiently penetrating radiation; for this reason, the large majority of WDM diagnostics are X ray photon-in photon-out measurements.

In the remainder of this section I provide an overview of the various available X-ray techniques.

1.3.1 Scattering

Elastic scattering and nonresonant inelastic X-ray scattering (NIXS) are among the most-frequently probed signals for inferring the structure, temperature and ionization state of WDM. In dense plasmas generated by long-pulse lasers, where LTE is commonly assumed, NIXS also serves as a probe of temperature.

For a given sample, the sum of scattering interactions is characterized by the double-differential scattering cross section (DDCS) $d^2\sigma/d\Omega d\omega$, which describes the probability of a photon to scatter into a solid angle increment $d\Omega$ within an energy loss interval $d\omega$. Within the independent-electron and first Born approximations the DDCS is given by

$$\frac{d^2\sigma}{d\Omega d\omega} = r_0^2 \left(\frac{\omega_2}{\omega_1} \right) |\epsilon_1 \times \epsilon_2^*|^2 S(\vec{q}, \omega), \quad (1.1)$$

where

$$S(\vec{q}, \omega) \equiv \sum_F \sum_j \langle F | \exp(i\vec{q} \cdot \vec{r}_j) | I \rangle |^2 \delta(E_F - E_I - \hbar\omega). \quad (1.2)$$

The first term in equation 1.3.1 is the Thomson cross section, which describes the interaction between a probe photon and a single electron; $S(\vec{q}, \omega)$ is referred to as the dynamic structure factor, and encapsulates all system-specific properties. I and F are initial and final states of the sample with energies E_I and E_F , respectively, and the second summation of 1.3.1 is over electrons in the scatterer.

Following Chihara (cite Chihara), the typical treatment of a dense plasma separates the dynamic structure factor into several components:

$$S(\vec{q}, \omega) = |f_I(q) + f_e(q)|^2 S_{ii}(q, \omega) + S_{ff}(q, \omega) + S_{bf}(q, \omega), \quad (1.3)$$

S_{ii} is the atomic/ionic structure factor, f_I and f_e are the form factors for the ion and a surrounding cloud of screening scharge. S_{ff} contains scattering from free, delocalized electrons, and S_{bf} represents Raman-type bound-free transitions resulting from scattering from tightly-bound core level electrons. Note that spherical symmetry has been assumed: all terms of the structure factor depend only on the magnitude of \vec{q} .

The first term corresponds to elastic ($\omega = 0$) scattering, and is connected to the dense plasma's pair distribution function by a Fourier transform. Though not a component of the NIXS signal, it must often be considered in simulations and analyses of NIXS data, wherein the Bethe sum rule (cite) and other conserved quantities consist of integrals over the entire energy-loss domain of the dynamic structure factor. Elastic scattering is a highly-useful probe of structure; we consider it separately in section 1.3.1.

The free-free contribution to $S(q, \omega)$ can be expressed in terms of the free-electron dielectric function $\epsilon(q, \omega)$ via the fluctuation-dissipation theorem (cite Kubo et al.):

$$S(q, \omega) = \frac{\epsilon_0 \hbar q^2}{\pi e^2 n_e} \frac{1}{1 - e^{\hbar \omega / k_B T_e}} \text{Im} \frac{1}{\epsilon(q, \omega)}, \quad (1.4)$$

The random phase approximation (RPA) (cite Bohm and Pines) is typically used as an approximation for $\epsilon(q, \omega)$, but more recent treatments incorporate a perturbative treatment of electron-ion interactions using the Born-Mermin Approximation (cite Mermin). As shown

in Fig. (which figure?), the scattering contribution of S_{ff} consists of a pair of Plasmon peaks with opposite, equal-magnitude energy offsets from the elastic scattering peak. Electron density is inferred from the magnitude of the Plasmon peak shifts while temperature is obtained from the ratio of intensities of the two peaks, following the principle of detailed balance (cite Glenzer 2007 and Lee 2009).

Although the connection of temperature and density to the free-free component of the dielectric function is well-founded, there are two obstacles to effective interpretation of collective scattering data from WDM systems; one is theoretical and the other experimental. First, the validity of established treatments of the dielectric function has been called into question, with recent plasmon spectrum calculations based on MD-DFT simulations showing a significant change in the plasmon profile compared to that predicted by the BMA. (cite Mattern thesis and Plagemann). Second, the plasmon peak suffers from poor signal to background and has a small separation from the elastic scattering peak under typical WDM electron densities, making it difficult to resolve. As a result only a handful of experiments to date have pursued this technique.

We finally turn our attention to the last term of 1.3.1, S_{bf} , whose contribution to the inelastic DDCS is often referred to as x-ray Thomson scattering (XRTS). Obtaining state variable information from a system's bound-free scattering contribution is dependent on the underlying model of electronic structure used; as a result, various treatments exist, including the Impulse Approximation (IA) of Eisenberger and Platzman, wherein the bound-free contribution to XRTS is equivalent to Doppler-broadened Compton scattering (cite Eisenberger and Platzman); the plane wave form factor approximation (PWFFA) of Schumacher (cite Schumacher), which attempts to extend the IA by incorporating electron binding energies; and calculation of matrix elements using a real space Green's function (RSGF) formalism applied to atomic clusters, as implemented in the atomic spectroscopy code FEFF (cite Mattern).

In current practice, measurement of the bound-free component of XRTS from WDM is performed in the large- q regime, where the Compton feature is broad and can be measured

using high-efficiency (but low-resolution) HOPG-based spectrometers (need cites for this). As such, single-particle bound-free scattering is more readily measured than collective excitation features. Since an early demonstration of the technique by Glenzer et al. (cite Glenzer 2003) it has been frequently implemented at both laser plasma and XFEL facilities (cite figures showing how these experiments are set up). Despite some fruitful outcomes (how so? need examples, cites), the large statistical uncertainties in XRTS spectra—particularly at laser plasma facilities, where single-shot measurements are photon-starved—make the inference of state variables difficult, and dependent on one’s choice of electronic structure model (check that this is right. do predictions heavily depend on the choice of model, or is it just that uncertainties are high, regardless of the choice?). Mattern et al. have demonstrated this concretely by comparing theoretical fits to XRTS data of shock-compressed Be, and argue that the lack of rigorous validation of electronic structure models for WDM models strongly undermines their validity for first-principles measurement of state variables. With this context as motivation, we revisit the topic of WDM thermometry in chapter (reference chapter).

1.3.2 Coherent Scattering

Coherent scattering is the zero-energy loss component of the double differential cross section. The inference of structural information from coherent scattering varies by material; two primary cases present themselves.

First, for amorphous materials, such as hot dense plasmas generated by ramp- or shock-compression and lacking long-range order, the scattering amplitude is isotropic and is characterized by the one-dimensional static structure factor, which is connected by a Fourier transform to the material’s pair correlation function. Inference of the full pair correlation function is in practice frustrated by the difficulty of inverting a limited momentum transfer range-sampling of the structure factor, but even in the most information-limited scenarios a density can nevertheless be recovered from the structure factor’s first correlation peak. Although coherent scattering measurements from dense plasmas have been demonstrated in

the context of long-pulse laser compression experiments, implementation difficulties unique to that environment prevent its adoption as a routine technique. We address these difficulties, and proposed solutions, in chapter (chapter reference). (cite Ma et al).

Second, in materials with long-range crystalline order, as typically found in XFEL-based experiments (whose timescales are shorter than the thermalization rate of electronic and ionic degrees of freedom), the coherent scattering amplitude is given by

$$F(\vec{q}) = \sum_n e^{i\vec{q} \cdot \vec{R}_n} \sum_j f_j(\vec{q}) e^{i\vec{q} \cdot \vec{r}_j}, \quad (1.5)$$

where the first summation is over all lattice vectors \vec{R}_n and the second, referred to as the *unit cell structure factor*, is over positions \vec{r}_j of atoms within the unit cell. By the convolution theorem, the crystal's scattering amplitude in reciprocal space is equal to the product of the lattice and unit cell structure factor. The coherent scattering signal is therefore a discrete sampling of the unit cell structure factor at individual Bragg peaks with momentum transfers corresponding to vectors of the reciprocal lattice.

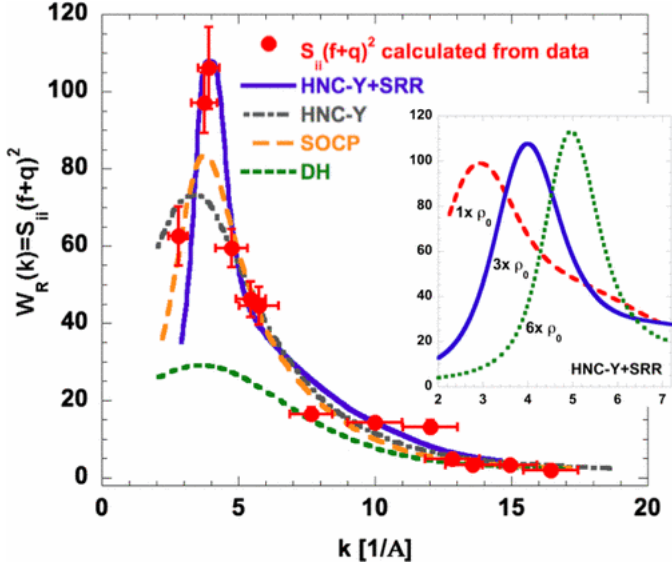
In the context of XRD from a material undergoing thermalization under fs XFEL heating, the crystal scattering amplitude's decomposition into lattice and unit cell components has a direct correspondence to interpretation of structural change. The onset of long-range lattice disorder is readily identifiable as a quenching in Bragg peaks roughly proportional to e^{-q^2} . Evolution of the unit cell structure factor, on the other hand, is dependent on the details of atomic level populations and the material's finite-temperature electronic structure, and can be used as a test of competing theoretical models of both.

(need cites and discussion of the existing literature on XRD of XFEL-heated WDM)

1.3.3 X-ray absorption

X-ray absorption spectroscopy (XAS) may be used to measure the structure and unoccupied electronic density of states of WDM systems. The information available by X-ray absorption near-edge spectroscopy (XANES) and X-ray absorption fine structure (XAES) is the same

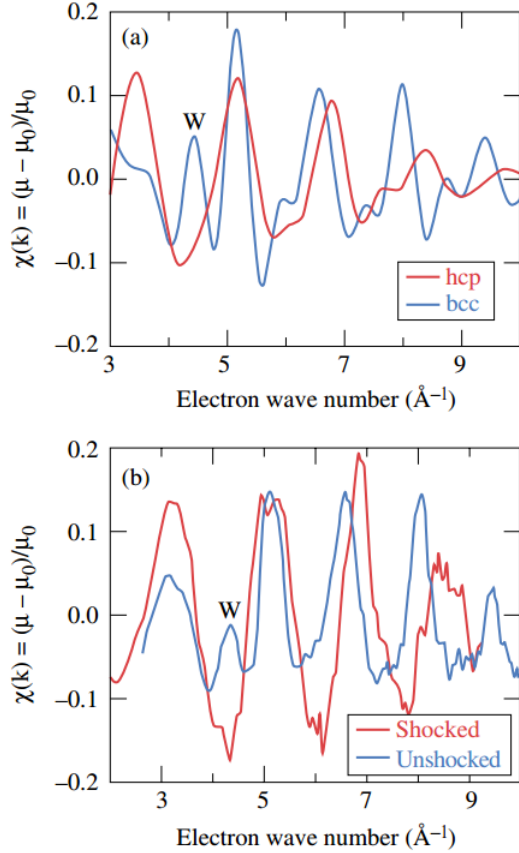
Figure 1.4: Experimental elastic scattering intensity of shock-compressed Al at OMEGA-60, compared to several hypernetted chain (HNC), Debye-Hueckel (DH), and screened one-component plasma (SOCP) models. (cite Ma et al.)



as in other scientific contexts, but the experimental implementation differs in a few respects. In all instances, the short duration of WDM states requires instantaneous collection of absorption spectra using a source with broad-band spectrum. At laser plasma facilities this is arranged using a spherical capsule of CH polymer imploded using a long-pulse laser (cite yaakobi 2003) that emits a thermal spectrum with a $\sqrt{1}$ MeV temperature (check this). This so-called broadband backscatter has been used to collect XAFS for the study of compression-induced phase transitions, such as that from bcc to hcp Fe driven by ns shock-compression (cite Yaakobi 2005).

XANES measurements on dense plasma have also been performed at laser plasma facilities. This requires narrower-band illumination compared with XAFS, which has been achieved using short pulse laser-driven multicomponent X-ray fluorescence backscatterers. Levy et al., for example, have used this technique to demonstrate XANES-based thermometry based on measurement of the K-edge slope in Al isochorically heated to 3 eV. (cite Levy et

Figure 1.5: FEFF calculation of XAFS for hcp and bcc phases of Fe (a), compared to experimental data taken on ambient and shock-compressed Fe at the OMEGA laser (b). (cite Yaakobi)

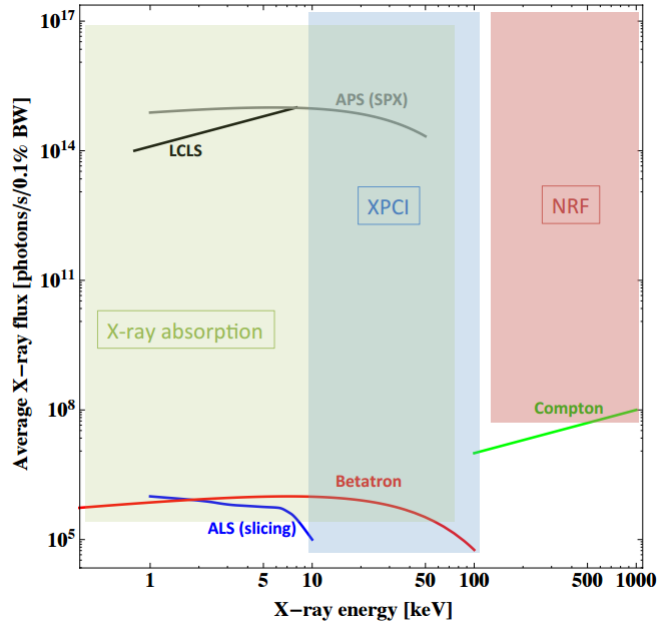


al).

Laser wakefield accelerator X-ray sources generate fs-duration broadband X-ray emission, affording time resolution that surpasses what is possible with laser-driven backscatterers. This makes wakefield accelerators especially well-suited to X-ray absorption spectroscopy of WDM generated at XFEL facilities (cite Albert). The combination of wakefield accelerators with XFELs promises the unprecedented possibility of XFEL pump-probe experiments with simultaneous fs-duration interrogation of the target using broad- and narrow-band hard X-rays. This combination also enables XAS measurements of low-Z materials, which is much

more challenging at laser plasma facilities as a result of the mismatch between the short penetration lengths of x-rays near the K-edges of low-Z species and the relatively large target thicknesses (tens of microns) needed for effective laser ablation.

Figure 1.6: Parameter spaces of several x-ray techniques (X-ray phase contrast imaging (XPCI), x-ray absorption, and nuclear resonance fluorescence (NRF)), overlaid with curves indicating the regions of parameter space accessible by various x-ray source technologies and individual facilities (cite Albert).

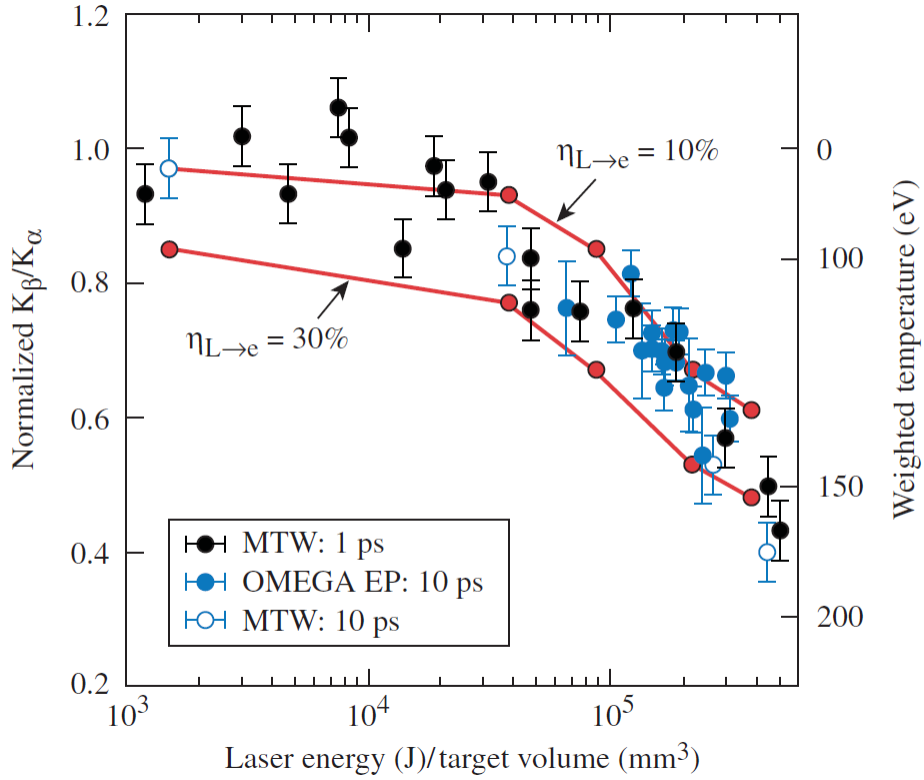


1.3.4 X-ray Emission and X-ray Fluorescence

X-ray fluorescence spectroscopy (XRF) is an extensively used probe in experiments studying the interaction of high-intensity lasers with solid targets. In short-pulse laser experiments involving mid-Z elements heated to temperatures comparable to or larger than M-shell binding energies the ratio of K_β to K_α emission is used as a measurement of temperature. Modeling the coupling efficiency between high-power laser and electrons in a solid-density target is of considerable significance to the effort to understand optical radiation-matter interactions

at high laser intensities ($> 10^{19} \text{ W/cm}^2$); in this context, inference of target heating using K_β/K_α branching ratios provides a useful consistency check in the application of models to experimental data. (cite Myatt et all 2007, Nilson).

Figure 1.7: Experimental K_α/K_β ratios of emission from Cu foil heated by short-pulse lasers, with inferred electron temperature on the right vertical axis. Model calculations are heating for hot electron coupling efficiencies η_e equal to 10% and 30% (cite Nilson)



X-ray emission spectroscopy (XES), the finer-grained cousin of XRF, provides more detailed information on the occupied density of states in a material and can be sensitive to valence-level excitations in the ‘tepid’ transitional regime between ambient and warm dense matter states (reference XES figure from the LD67, maybe get some cites). It has seen use primarily at XFEL facilities, where higher shot rates and probe intensities make the collection of datasets with satisfactory statistical quality easier. (cite photosystem 2 XES

papers). The advent of XFELs as the first high-intensity, monochromatic, and tunable WDM probes has also enabled resonant inelastic X-ray scattering (RIXS) measurements, which has made possible the direct measurement of ionization potential depression on a fs timescale, as demonstrated by Vinko et al. (cite Vinko, Cricosta.).

1.4 *Dissertation Outline*

The overarching theme in this thesis is the relationship, and frequent feedback, between scientific discovery and the development of new experimental technique. To begin, in chapter 2 I introduce a scheme for single-shot measurement of the static structure factors of disordered dense plasmas produced at large-scale laser facilities such as Omega and NIF. In Chapter 3 I present an experimental observation of nonlocal heat transport by keV-scale electrons in a nanophase material and consider the question of how this effect can be used to improve WDM experiments conducted at XFELs via optimized nanostructured target design. In chapter 4 I discuss experimental results of a recent experiment at the LCLS in which we established bounds on the timescales for thermalization of the lattice in XFEL-heated metal oxides and measured the consequences of XFEL heating on electronic charge density, with subsequent comparisons to different model predictions. In chapter 5 I describe an instrument-development effort toward a disposable CMOS-based X-ray camera for use in experimental environments hostile to electronics, particularly laser plasma facilities. Finally, in chapter 6 I introduce UW-XAP, a software tool for streamlined realtime data collection and analysis at the LCLS.

Chapter 2

PHYSICS OF PENELOPE

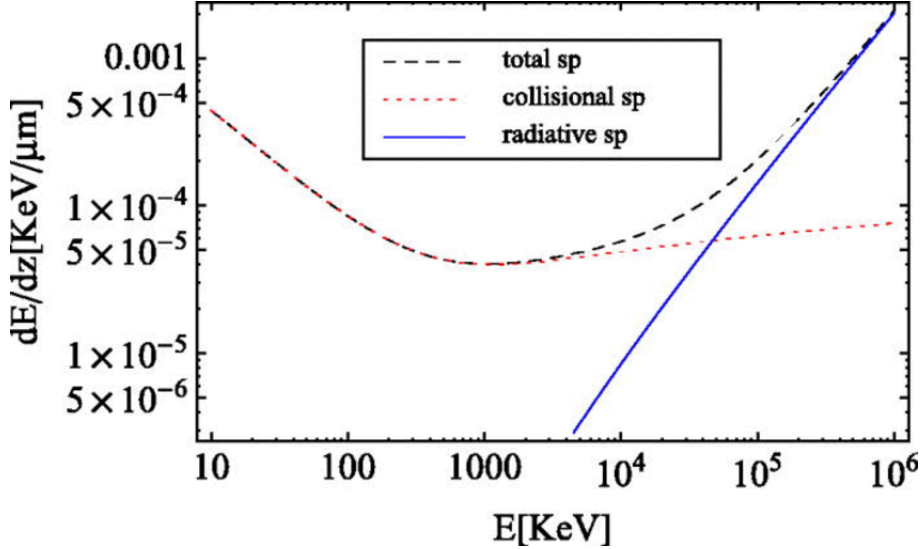
PENELOPE performs Monte Carlo simulations of coupled electron-photon transport in arbitrary materials in the energy range of 100 eV to 1 GeV. It uses a mixed simulation method that treats soft interactions (that is, those involving small angular deflections) with a multiple-scattering approach while individually simulating hard interactions. It is paired with a geometry-definition program, PENGEOM, that allows defining samples with volumes of different material composition separated by arbitrary quartic surfaces.

2.1 Types of interactions

In this section we consider the interactions that must be simulated to accurately model the spatial distribution of energy in a nanostructured target material heated by x-ray photons with energy on the order of 10 keV. PENELOPE simulates the following interactions: electron scattering (elastic and inelastic), Bremsstrahlung emission, photon scattering (both elastic (Rayleigh) and inelastic (Compton)), photoelectric absorption and Auger emission, x-ray fluorescence, and pair production and annihilation. Figs. 2.1 and ?? show the energy dependence of the relative strengths of the above electron and photon interactions, respectively. Several of the processes have negligible or nonexistent roles on the $\downarrow 10$ keV energy scale considered in the current work, allowing us to limit our scope to the electron scattering and photoabsorption (with consequent fluorescence and Auger emission).

In what follows we introduce the physics of photoabsorption and elastic and inelastic scattering with attention to each process's contribution to the spatial distribution of deposited energy in a relaxation cascade beginning with photoionization by a hard x-ray photon. We discuss standard modeling approaches relevant to the 100 eV-10 keV regime, in addition

Figure 2.1: Collisional and radiative electron stopping powers as a function of energy (cite)

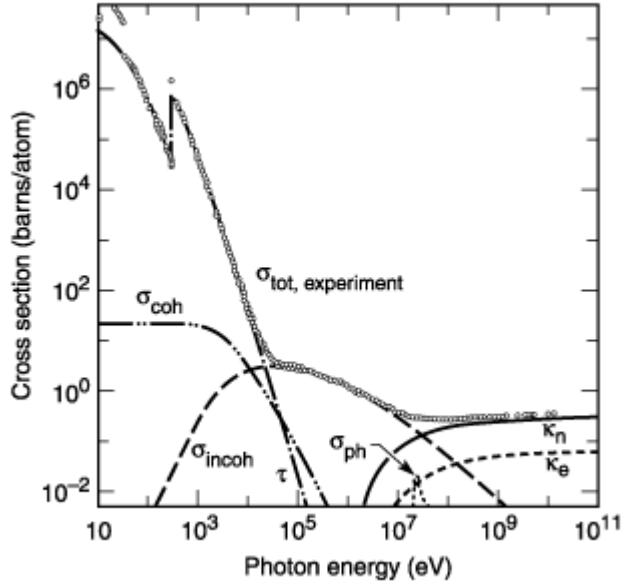


to cursory overviews of PENELOPE's treatments within the limited scope relevant to the current regime of interest.

2.1.1 Fluorescence

Fig (insert fig. 2.2 from penelope manual) illustrates the photoionization of inner atomic shells and introduces the notation used to describe atomic energy levels and transitions between them. Both the photoelectric effect and secondary (Auger) emission resulting from high-energy atomic excitations can be accurately modeled using established treatments that combine theoretical calculation of atomic states via self-consistent modeling (cite Pratt et al. 1973) with experimental data. Associated quantities are compiled in databases; PENELOPE uses tabulated ionization energies from Carlson (cite Carlson et al.) and photoelectric cross sections from the LLNL Evaluated Photon Data Library (EPDL). The EPDL additionally provides emission probabilities for fluorescence photons and Auger electrons in the relaxation of ionized atoms to the ground state.

Figure 2.2: Photon cross section components in C as a function of energy (cite LCL and Hubbell 1980)



Assumptions

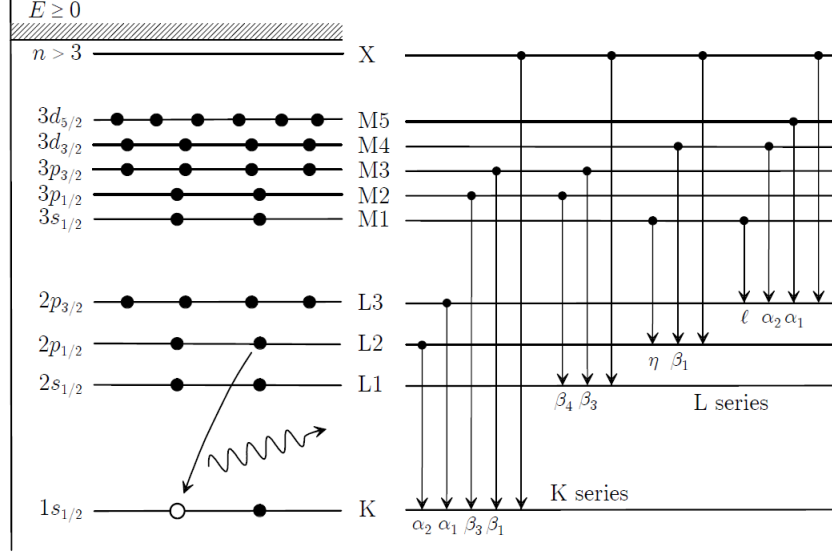
The above data sources are known to be accurate to the 1% level above 1 keV, under the condition (assumed by PENELOPE) of low incident photon densities, such that only single-electron transitions occur (cite PENELOPE manual).

PENELOPE assumes that incident photons are unpolarized and consequently fails to reproduce the polarization-dependent angular distribution (cite?) of emitted electrons. We note that it does incorporate the angular distribution from Sauter's (cite sauter 1931) treatment of relativistic photoelectron emission—which, however, reduces to isotropic emission in the nonrelativistic regime covered here.

2.1.2 Elastic scattering

Elastic scattering of electrons refers to interactions that do not alter target atoms' states.

Figure 2.3: Atomic energy levels of the first three principal quantum numbers (left) and corresponding allowed radiative transitions (right).



The simplest widely-used model for elastic scattering of electrons in a solid is the semi-classical approach of Wentzel and Lenz (Egerton page 114), known as the Lenz model, which uses the Yukawa potential for the interaction between a fast electron and a target atom:

$$V(r) = \alpha^2 \frac{e^{-r/r_0}}{r} \quad (2.1)$$

The first Born approximation gives the amplitude for a particle's scattering off of a spherically symmetric potential as

$$f(\theta) \simeq -2 \frac{m}{\hbar^2 q} \int_0^\infty r V(r) \sin(qr) dr \quad (2.2)$$

Substituting (how do I reference equations) into (), yields

$$f(\theta) \simeq -2 \frac{m \alpha^2}{\hbar^2 q} \int_0^\infty e^{-r/r_0} \sin(qr) dr = -\frac{2m \alpha^2}{\hbar^2 (r_0^{-2} + q^2)}, \quad (2.3)$$

therefore giving the following differential scattering cross section:

$$\frac{d\sigma}{d\Omega} = |f(\theta)| = \frac{4Z^2}{a_0^2 k_0^4} \frac{1}{(\theta^2 + \theta_0^2)^2},$$

where $k_0 = m_0 v$ is the momentum of the incident electron, $\theta_0 = (k_0 r_0)^{-1}$ is the characteristic angle for elastic scattering and $a_0 = 4\pi\epsilon_0\hbar^2/m_0e^2$ is the Bohr radius.

Using the Thomas-Fermi model, Wentzel and Lenz obtain $r_0 = a_0 Z^{-1/3}$ (cites). Doing this substitution and integrating over scattering angles gives

$$\sigma_e = \int_0^\pi \frac{d\sigma}{d\Omega} 2\pi \sin\theta d\theta = \frac{4\pi}{k_0^2} Z^{4/3} \quad (2.4)$$

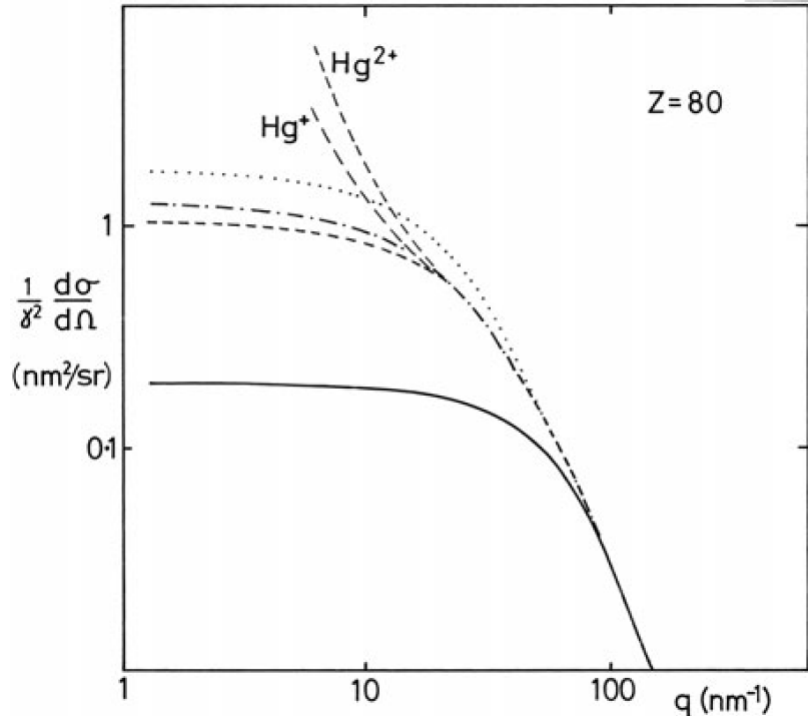
We thus see that the angular deflections produced by elastic scattering decrease with increasing energy. For 10 keV electrons $\theta_0 \simeq 0.1$ rad and $\sigma_e = 4.2 \times 10^{-20} \text{ m}^2$. The elastic mean free path, an alternate measure of the collision frequency, is equal to $\lambda_e = 1/(\sigma_e n)$, where n is atomic number density. As an example, inserting the value of n for Fe yields 2.8 Å(at the same 10 keV electron energy) (*sounds far too small; check this calculation*). This corresponds to a large number of collisions on length scales of interest ($\gtrsim 10 \text{ nm}$) which, combined with the appreciable value of the characteristic scattering angle, demonstrates that elastic scattering has a substantial influence on the propagation of electrons below 10 keV.

Taking the atomic number of density of Fe, the mean free path between inelastic collisions is (insert the right expression) = (insert the right number). The corresponding expectation value of angular deflection per distance traveled is (insert the right number). In comparison, the inelastic mean free path of 10 keV photons in Fe (potential see-saw here is (insert number). where should i introduce inelastic scattering?) This suggests that path deflections caused by elastic scattering will have a significant influence on the spatial distribution of energy deposited 10 keV-scale electrons in Fe and other mid-Z materials.

Despite its simplicity, the Lenz model gives total cross sections to within 10 % for light elements (cite Geiger 1964). For heavier species it underestimates the small-angle differential cross section (Fig. 2.4) but correctly reproduces the large-angle DCS.

More accurate approaches use iterative (e.g. Hartree-Fock) solutions to the Schrödinger equation (or of the Dirac equation, where relativistic and spin effects are needed) to solve for the atomic potential. (cite rez 1984 or starostin, applicability of the born approximation to collisions between electrons and excited atoms). Additionally, partial wave approaches can

Figure 2.4: Angular dependence of elastic DCS of 30 keV electrons from a Hg atom under the Lenz model using the Wentzel potential (solid), and based on Hartree-Fock (dotted), Hartree-Slater (dot-dashed) and Dirac-Slater (dashed) wavefunctions. (**Reference1**)



be used to avoid the Born approximation in regimes for which it fails (low electron energy and high-Z species). PENELOPE combines the above techniques: it solves the partial-wave expanded Dirac equation with a potential based on the Dirac-Fock electron density of Desclaux (1975, see citation on pg 102 of penelope manual) and exchange interaction of Furness and McCarthy (1973). We will elaborate on PENELOPE's modeling of elastic scattering only within the narrow concern of assessing its range of applicability; for more detail the reader may refer to chapter 3 of the PENELOPE manual.

2.2 Inelastic scattering

Inelastic collisions are the dominant mechanism for energy loss of electrons up to above 10 keV (2.1).

In an atomic system, the differential cross section for a transition from initial state wavefunction ψ_0 to final state wavefunction ψ_n is

$$\frac{d\sigma_n}{d\Omega} = \frac{m_0}{2\pi\hbar^2} \frac{k_1^2}{k_0} \left| \int V(r) \psi_0 \psi_n \exp(iqr) d\tau \right|^2 \quad (2.5)$$

where \mathbf{k}_0 and \mathbf{k}_1 are the wave vectors of the incident electron before and after scattering and $q = \hbar(\mathbf{k}_1 - \mathbf{k}_0)$ is the corresponding momentum transfer.

At nonrelativistic velocities the potential between electron and atom may be expressed as the following sum of Coulomb potentials of the nucleus and atomic electrons:

$$V(r) = \frac{Ze^2}{4\pi\epsilon_0 r} - \frac{1}{4\pi\epsilon_0} \sum_{j=1}^Z \frac{e^2}{|\mathbf{r} - \mathbf{r}_j|} \quad (2.6)$$

Substituting the second term of equation 2.6 into 2.5, we note that the nuclear potential is independent of the coordinates of the atomic electrons and can therefore be removed from the integral. The orthogonality of the wave functions ψ_n implies that the nuclear potential does not contribute to inelastic scattering; the expression for the differential cross section of inelastic scattering is therefore:

$$\frac{d\sigma_n}{d\Omega} = \left(\frac{4}{a_0^2 q^4} \right) \frac{k_1}{k_0} |\epsilon(q)|^2, \quad (2.7)$$

where

$$\epsilon_n = \int \psi_n \sum_j e^{iqr_j} \psi_0 d\tau. \quad (2.8)$$

The generalized oscillator strength is an important related quantity:

$$f_n(q) = \frac{E_n}{R} \frac{|\epsilon_n(q)|^2}{(qa_0)^2}, \quad (2.9)$$

where $R = (m_0 e^4 / 2)(4\pi\epsilon_0\hbar)^{-2}$, the Rydberg energy, and E_n is the energy change of the transition.

The GOS is in general continuous and therefore better expressed as a density with dimensions 1/energy, i.e. $df(q, E) / dE$. This allows us to write the double-differential cross section of inelastic scattering:

$$\frac{d^2\sigma}{d\Omega dE} = 4REq^2 \frac{k_1}{k_0} \frac{df}{dE}(q, E), \quad (2.10)$$

TODO: calculate a typical inelastic scattering cross section for comparison elastic scattering. The fact that the ratio is of order unity demonstrates that both matter.

2.2.1 Dielectric function

While this formulation makes it possible to calculate the GOS and associated quantities starting from an atomic model, in solid state systems the scattering cross section of outer-shell bonding is influenced by collective effects and chemical bonding. It's therefore preferable to describe the inelastic scattering of an electron off a solid using the solid's dielectric response function, $\epsilon(q, E)$.

Ritchie (cite Ritche 1957) showed, using Poisson's equation and fourier transforms, that an electron moving in the z-direction in an infinite medium experiences a force of the following magnitude opposite its direction of motion:

$$\frac{dE}{dz} = \frac{2\hbar^2}{\pi a_0 m_0 v^2} \int \int \frac{q_y \omega Im[-1/\epsilon(q, \omega)]}{q_y^2 + (\omega/v)^2}, \quad (2.11)$$

where q_y is the component of the momentum transfer vector perpendicular to v and $\omega = E/\hbar$ is an angular frequency. This quantity is referred to as the stopping power. It can be expressed in terms of the previously-defined DDCS:

$$\frac{dE}{dz} = \int \int nE \frac{d^2\sigma}{d\Omega dE} d\Omega dE, \quad (2.12)$$

where E is energy loss and Ω is solid angle. By equating equations 2.11 and 2.12 in the small-angle limit it can be shown, by comparison with the atomic treatment (cite), that

$$\frac{df}{dE}(q, E) = \frac{2E}{\pi E_a^2} Im\left[\frac{-1}{\epsilon(q, E)}\right],$$

thus demonstrating the equivalence of the atomic and dielectric approaches.

Note, finally, that the GOS fully determines the the value of equation 2.10 within the first Born approximation. As such, given the potential of equation 2.5 all modeling of the inelastic scattering of electrons at intermediate energies (1 keV - 300 keV) reduces to construction of a GOS model.

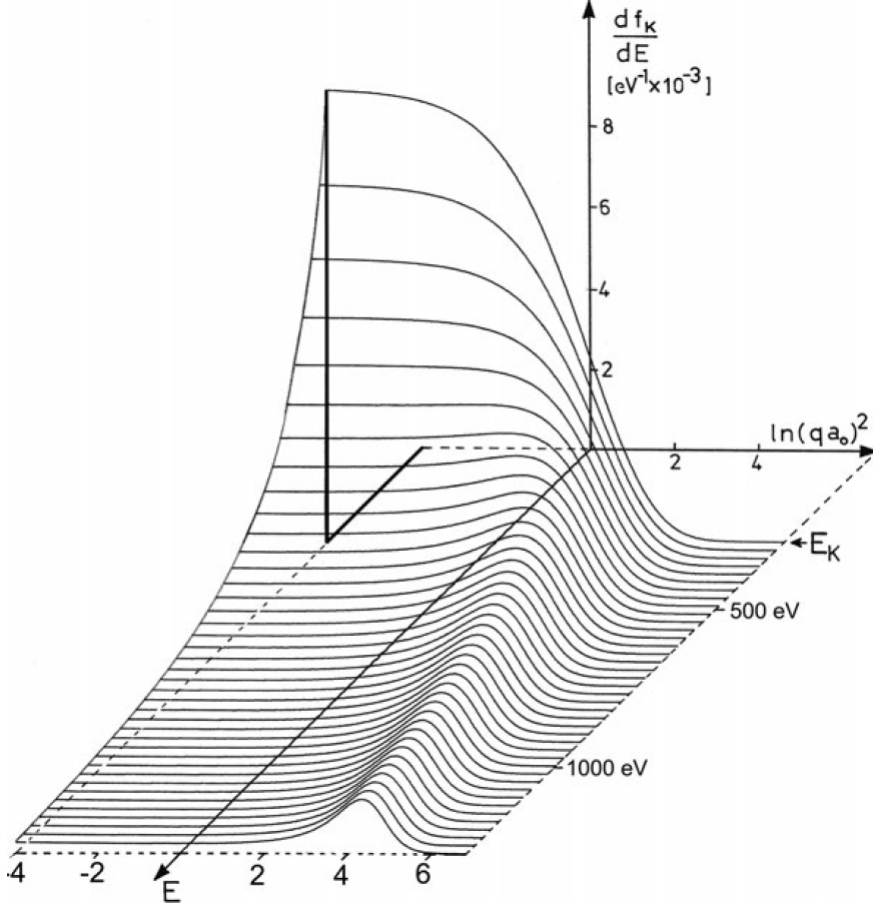
2.2.2 Modeling the generalized oscillator strength

Analytical expressions for the GOS are known for only two simple cases of the free electron gas and hydrogen atom. In practice, however, it has been shown that the physics of inelastic scattering is mostly determined by a few global features of the GOS (cite Salvat and Fernandez-Varea, 1992) and that relatively simple models are therefore adequate in most situations.

The GOS is conventionally represented as a two-dimensional surface plot called the Bethe surface (Fig. 2.5). We identify two constraints on the behavior of the Bethe surface which any GOS model must reproduce. First, in the limit $Q \rightarrow 0$, the GOS of the dielectric formulation becomes proportional to the optical oscillator strength $Im[-1/\epsilon(0, E)]$, which is experimentally constrained by x-ray emission measurements. Second, in the limit of large momentum transfer the most probable energy loss is equal to the kinematically-determined value for collision between two free electrons, $E = q^2/2$. (cite Sorini). The corresponding trace in energy and momentum is a feature of the Bethe surface known as the Bethe ridge.

As in Compton scattering, the shape of cuts through the Bethe surface (i.e. spectra of scattered intensity as a function of energy at fixed momentum transfer) is determined by the momentum distribution of atomic electrons. Certain models, such as that of Sorini et al

Figure 2.5: Bethe surface for ionization of the K shell in C..... (cite)



(cite sorini 2006), derive a value for the width of the Bethe ridge from Fermi velocity calculations. PENELOPE adopts a simpler form based on the ‘ δ -oscillator’ model of Liljequist (cite Liljequist 1983) which splits the GOS into contributions from generalized ‘shells’ (each corresponding to either an atomic shell or a collective excitation). The total GOS under this model is a sum over indices k of the shells:

$$\frac{df(q, E)}{dE} = \sum f_k [\delta(E - E_k) \Theta(q_k - q) + \delta(E - q) \Theta(q - q_k)],$$

where for the k th shell f_k is the shell’s number of electrons, q_k is the cutoff recoil energy, and E_k is the shell’s resonance energy. Q_k is equal to the shell’s binding energy U_k (excluding

the band, for which it is set to 0), and E_k is computed from from U_k and the material's mean electron density, following Sternheimer (cite Sternheimer 1952). Within this model the GOS is fully determined by the shells' occupations and cutoff (binding) energies U_k , which PENELOPE obtains from Carlson (cite Carlson 1975). It is possible, optionally, to direct PENELOPE to fit its GOS model to experimental stopping power data provided in material input files. It performs this fit through reweighting of the GOS model's oscillators (*this is actually a guess, as the PENELOPE manual is totally opaque about how the GOS/DDCS is fit to stopping power input data. Better understanding would require me to revisit PENELOPE's code or contact the authors*).

Substantial additional detail on the construction and interpretation of PENELOPE's GOS model can be found in its manual.

2.3 Accuracy and useful regimes

In the context of simulation of nanostructured materials, errors in PENELOPE's DCSs for electron scattering originate from both (1) the limited range of validity of PENELOPE's physical models with respect to the bulk properties PENELOPE seeks to reproduce, and (2) from the difference between scattering DCSs of ambient-condition bulk materials on the one hand and high-temperature nanostructured materials on the other. We address these two issues in combination.

As mentioned previously, a material's inelastic scattering DCS is fully determined by its loss function, the imaginary component of the dielectric function. Any difference between the responses of bulk and nanophases arises from the contribution to the loss function of collective electronic excitations, i.e. plasmons. Plasmon modes in nanostructured materials form a large research topic on their own (find and cite review article on surface plasmons in nano-materials), but there has been little (no?) (cites) prior work in the context of high-temperature dense matter. The study of heated nanophase materials thus manifests itself as both a problem and an opportunity. On the one hand, the lack of experimental data and accurate modeling makes it impossible to fully quantify the inaccuracy of simula-

tions of ambient, bulk materials. On the other hand, XFEL heating experiments could be used to discriminate between computed dielectric response functions and their underlying finite-temperature electronic strucure theory—to the extent that alternative models generate experimentally measureable differences in inelastic DDCSs. We thus suggest that XFEL heating of nanostructured materials could enable a joint modeling/experimental program to validate WDM electronic structure theory.

2.3.1 Low-energy loss DCS

In the current situation, wherein the plasmon contribution to the loss function is not known, we can take advantage of the fact that plasmon resonance are confined to energy losses smaller than approximately 100 eV. The influence of the low-energy region of the loss function on the spatial distribution of deposited energy can therefore be bounded using the continuous slowing down approximation (CSDA) of 100 eV electrons. The CSDA for electrons of energy E_0 is the following integral over stopping power:

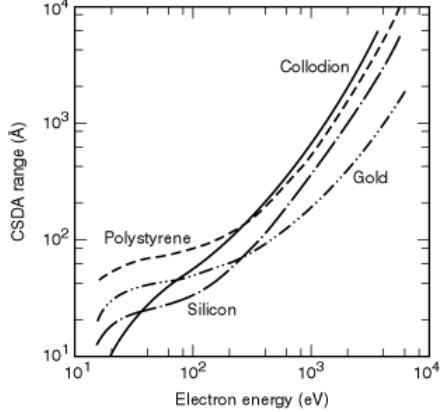
$$l_{CSDA} = \int_{E_{final}}^{E_0} \left(\frac{dE}{dz} \right)^{-1},$$

where E_{final} , the final energy of the electron, is usually taken to be 10 eV. For elements heavier than boron, $l_{CSDA} < 10$ nm for $E = 100\text{eV}$. We therefore conclude that inaccuracy in treatments of collective excitations affect the spatial distribution of energy deposited by electrons on a length scale below 10 nm (Fig. 2.6)

2.3.2 Energy cutoffs

PENELOPE stops simulation of an electron's motion once its energy drops below a prescribed cutoff value; at the endpoint of an electron's simulated track all of the electron's final energy is deposited at its final position. The resulting distortion in the spatial distribution of deposited energy can be bounded, as above, using the CSDA. PENELOPE's cutoff energy can be set as low as 50 eV. Assuming this value is chosen, the resulting error is much smaller

Figure 2.6: CSDA range as a function of energy for several materials, based on stopping powers of..... (cite)



than the bound from section 2.3.1 on the error attributed to inaccuracy in the low-energy dielectric function. Simulation error due to PENELOPE’s energy cutoff can therefore be safely neglected.

2.3.3 Elastic scattering

PENELOPE’s use of the static field approximation in its elastic scattering model introduces a low-energy error in the DCS due to the effect of the polarizability of atomic charge (cite Salvat 2003). The size of this error is 20% at 1 keV and 50% at 100 eV (PENELOPE manual, pg. 102). The CSDA range at 1 keV, where uncertainty at the DCS level is considerable, ranges from 10 nm for high-Z elements to over 100 nm for low-Z ones. Because the results of the PENELOPE simulations discussed in chapter (which chapter?) are sensitive to errors on the 10 nm - 100 nm length scale, the CSDA does not usefully constrain the elastic DCS model’s contribution to uncertainty in the spatial distribution of deposited energy.

A crude estimate taking into account the magnitude of uncertainty in the elastic DCS may be obtained by considering elastic scattering of an electron as a correlated random walk. Given a mean free path λ_e and characteristic scattering angle θ_0 , the number of steps after which the electron’s direction of motion becomes uncorrelated with its initial direction is of

the order $n = \pi/\theta_0\lambda_e$. The number of elastic scattering events an electron experiences as it slows from an energy of 1 keV to 100 eV (the previously-established—but arbitrary—cutoff below which the treatment of section 2.3.1 applies) is

sketch: basically I have to calculate the number of scattering events, and associated dephasing of the electron’s direction, for several ‘bins’ of energy between 100 eV and 1 keV. For each bin we calculate the equivalent number of steps under an uncorrelated random walk. This yields an expected displacement proportional to the square root of the number of steps in the uncorrelated random walk, which we can multiply by the elastic DCS uncertainty in order to get an associated displacement uncertainty. All displacement uncertainties can then be added in quadrature, yielding a final uncertainty.

2.4 Inelastic scattering

Inelastic scattering has much smaller characteristic angles than elastic scattering scattering but comparable total cross sections. As a result the influence of angular deflections by inelastic scattering on the propagation of electrons is relatively small. The effect of uncertainties in the inelastic scattering DDCS can thus be neglected, and we confine our attention to uncertainty at the level of the stopping power, a more coarse-grained quantity.

Fig 2.7 compares PENELOPE’s computed stopping powers and inelastic mean free paths (for what???) to several experimental datasets. The level of disagreement between different datasets is of the order 2 in the 1 keV - 10 keV energy loss range; the discrepancy between PENELOPE’s modeled stopping power and the experimental datasets is also of this order. Because all transport lengths are proportional to stopping power we must thus contend with a factor of 2 uncertainty in the length scale of computed spatial distributions—far larger than any of the other uncertainties we have considered until now.

The conclusions of chapter (WHICH CHAPTER?) can nevertheless be conserved, with one modification, if we consider PENELOPE’s error in modeling the 1 - 10 keV stopping power as an unknown constant-factor scaling in stopping power. Such an uncertainty corresponds to an unknown scaling of both (1) the length scale of spatial distributions of deposited

energy and (2) the flux magnitude of nonlocally-transported energy crossing a given material interface. To give a simple illustration, consider a one-dimensional configuration consisting of an infinite extent of source material from $x = -\infty$ to $x = \infty$. When the sample receives x-ray illumination of magnitude unity at position x_0 the density distribution $\rho(x)$ of deposited energy is given by a response function $f(x)$ (fully determined by the sample material's stopping power and incident x-ray spectrum): $\rho(x) = f(x - x_0)$. If the material is uniformly illuminated by x rays in the region spanning $x = 0$ to $x = \infty$ then (in arbitrary units):

$$\rho(x) = \int_0^\infty f(x - x')dx'.$$

Under the substitution $f(x) \rightarrow g(x) = f(cx)$ (equivalent to scaling $dE/dz \rightarrow (1/c)dE/dz$ of the stopping power), and maintaining normalization of the response function, the distribution becomes:

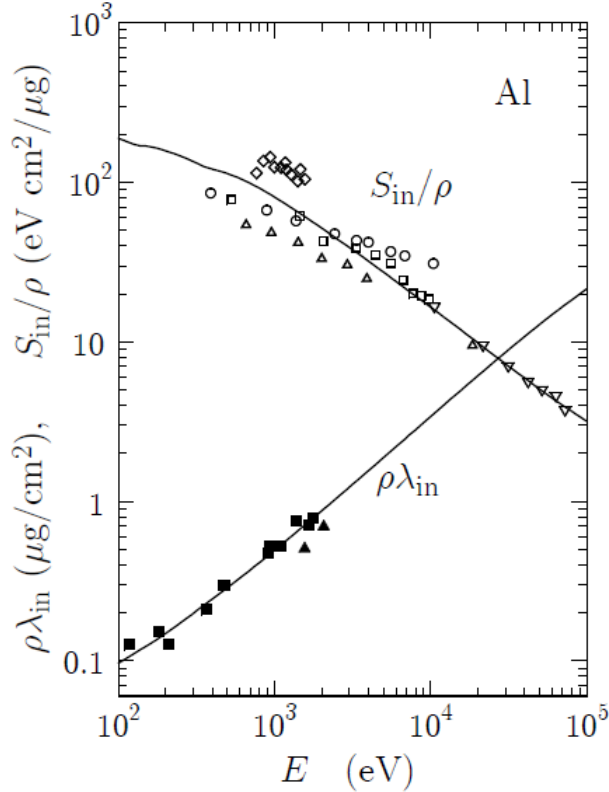
$$\rho'(x) = \int_0^\infty cf((c(x - x')))dx = \int_{cx}^\infty f((u))u.$$

Therefore constant-factor scaling of the stopping power is equivalent to a change in units of length, implying that, under our assumed form of the uncertainty in dE/dz , and adding the assumption that the unknown scaling factor c is equal for all materials, the simulated spatial distributions of deposited energy density are correct up to a uniform scaling of the sample geometry.

2.5 Dosimetry

PENELOPE's dosimetry includes both linear energy transfer from radiation to matter and the contribution of particle track ends, as mentioned in section 2.3.2. At the energy scales of interest the former contribution may be neglected, and the distribution of energy deposited by a particle shower is entirely dependent on simulated inelastic scattering events. PENELOPE's dosimetry calculation is tied to the termination of electron tracks: when an electron's energy drops below the (previously-defined) cutoff value its simulation ceases, and

Figure 2.7: Stopping power and inelastic mean free path for electrons as a function of energy in Al..... (cite)



its entire energy is deposited at the track's endpoint. Similarly, the energy loss of soft inelastic collisions (ones having energy loss greater than the cutoff energy W_{cc}) is deposited locally (whereas hard inelastic collisions generate secondary electrons that are individually tracked).

Coarse-graining of the dose distribution is done by dividing the simulation volume into a three-dimensional grid of cells, in each of which PENELOPE calculates the total dose of deposited energy. This grid is defined by the parameters GRIDX, GRIDY, GRIZ and GRIDBN in PENELOPE's input.

Chapter 3

A PHOTOMETRIC STUDY OF ENERGY-DISPERSIVE X-RAY DIFFRACTION AT A LASER PLASMA FACILITY

O.R. Hoidn and G.T. Seidler^(*)

Physics Department

University of Washington

Seattle WA 98195-1560

Abstract

The low repetition rates and possible shot-to-shot variations in laser-plasma studies place a high value on single-shot diagnostics. For example, white-beam scattering methods based on broadband backlighter x-ray sources are used to determine changes in the structure of laser-shocked crystalline materials by the evolution of coincidences of reciprocal lattice vectors and kinematically-allowed momentum transfers. Here, we demonstrate that white-beam techniques can be extended to strongly-disordered dense plasma and warm dense matter (WDM) systems where reciprocal space is only weakly structured and spectroscopic detection is consequently needed to determine the static structure factor and thus the ion-ion radial distribution function. Specifically, we report a photometric study of energy-dispersive diffraction (ED-XRD) for structural measurement of high energy density systems at large-scale laser facilities such as OMEGA and the National Ignition Facility. We find that structural information can be obtained in single-shot ED-XRD experiments using established backlighter and spectrometer technologies.

(*) Corresponding author: *seidler@uw.edu*

3.1 I Introduction

In addition to their centrality for inertial confinement fusion studies,^{1, 2} laser-shock experiments play a growing role at the interface between plasma physics and condensed matter physics, geosciences, and laboratory astrophysics.³⁻¹⁴ However, for experiments reaching the highest energy density states the technical challenges extend beyond the creation of such states: the low repetition rates, limited facility access, and significant shot-to-shot variations each place a special emphasis on single-shot x-ray diagnostics of the structural and electronic properties of the compressed, heated target.¹⁵⁻²⁴ An important case-in-point is provided by the determination of the ion-ion radial distribution function, $g_{ii}(\vec{r})$, or equivalently the static structure factor $S(\vec{k})$. Knowledge of $g_{ii}(\vec{r})$ fulfills an interesting variety of roles. First, it is necessary, if only at the level of mean density and average ionization state, for investigation of any equations of state (EOS) and of molecular dynamics simulations or other structural calculations performed in support of EOS calculations. Second, it is also a critical input parameter to any fine treatment of electronic structure. The electronic structure of dense crystalline systems and plasmas, in turn, is a quantity of fundamental interest but also of a certain pragmatic interest: some sufficient knowledge of electronic structure is needed for reliable determination of the target temperature and ionization state in dense plasma and warm dense matter (WDM) experiments^{25, 26}, and this capability is in turn needed for campaigns to experimentally measure the EOS in the WDM regime²⁷⁻²⁹.

For targets that retain substantial medium- or long-range order upon shock compression, broadband backlighter x-ray sources enable white-beam angle-dispersive x-ray diffraction (AD-XRD) in which substantial structural detail can be inferred from Kossel rings³⁰ and other fine scattering patterns dictated by the coincidence of reciprocal lattice vectors and kinematically-allowed momentum transfers^{31, 32}. However, white-beam AD-XRD is only applicable to systems that are substantially single crystalline: any statistically isotropic system, whether a polycrystalline fine-powder sample or a dense, partially ionized plasma, when illuminated by a broad-band source will show an angularly-featureless signal when

observed on, *e.g.*, an image plate. For high atomic number (Z) systems, single-shot white-beam extended x-ray absorption fine structure (EXAFS) has seen some applications³³; the situation has proven more challenging for lower- Z WDM and dense plasmas, as a result of the mutually-exclusive target thickness requirements of the x-ray measurement (soft x-ray penetration lengths of order 1 micron or less) and laser ablation (necessary thicknesses of tens of microns)³⁴. Consequently, the first determination of $g_{ii}(r)$ for disordered, dense lower- Z plasma systems³⁵ instead used multi-shot, quasi-monochromatic AD-XRD, *i.e.*, ‘traditional’ XRD.

Here, we investigate whether single-shot, white-beam XRD can be performed on *strongly disordered*, laser-shocked solids and WDM using spectral information at the detector location to parameterize the momentum transfer of the quasielastic scattering event, *i.e.*, we consider purely energy-dispersive x-ray diffraction (ED-XRD). Some context is needed to fully define this term and to distinguish it from XRD methods already in use in the laser-plasma community. The differential scattering cross section per atom for coherent scattering of x rays (ordinary diffraction of incoherent incident photons) from an isotropically disordered, elemental material such as a powder sample, liquid, or dense laser-shock heated plasma of a single atomic species is

$$\frac{d\sigma_{coh}}{d} (k) = \sigma_t S(k) f(k)^2 \quad (1)$$

where σ_t is the Thomson cross section, $S(k)$ is the directionally-averaged structure factor and $f(k)$ is the spherically averaged atomic form factor. The structure factor $S(k)$ is simply related by a sine transform to $g_{ii}(r)$,

$$S(k) = 1 + (4 \pi \rho/k) \int_0^\infty dr r [g_{ii}(r) - 1] \sin(kr). \quad (2)$$

These well-known expressions establish the close connection between XRD and $g_{ii}(r)$ while also demonstrating the need to measure the differential scattering cross-section (and hence $S(k)$) at many different momentum transfers if any significant constraint on the form of $g_{ii}(r)$ is to be obtained.

The k -dependence of $d\sigma_{coh}/d\Omega$ can in principle be measured with any suitable combinations of scattering angle 2θ and photon energies spanning the needed momentum trans-

fers: k is chosen by the combined effect of these two experimentally-selectable parameters, $k = (2E/c)\sin 2\theta$. In practice, however, XRD is measured in only two modes: angle-resolved XRD (henceforth ‘AR-XRD’) and energy-dispersive XRD (henceforth ‘ED-XRD’). Their distinction is best introduced kinematically. As illustrated in Fig. 3.2.1, any measurement of $S(k)$ must follow a curve in E - 2θ space which crosses many of the shown contours of constant k . The parameter space probed by a typical AR-XRD experiment using ~ 8 keV monochromatic incident photons is represented by the vertical curve in the figure. Experimentally, the necessary apparatus will include a monochromatic source and either an angle-scanning detector or a position sensitive detector (PSD), which we show schematically in Fig. 3.2.3 (a) and (b). On the other hand, a typical ED-XRD experiment instead resides on the horizontal curve in Fig. 3.2.1, *i.e.*, at a fixed scattering angle of 135 degrees but requiring both a broad incident source spectrum and an energy-resolving detector. An experimental schematic for ED-XRD is presented in Fig. 3.2.3(c). We note that ED-XRD has a long history in laboratory and synchrotron XRD studies, and plays an important role in high-pressure diamond anvil cell research where the limited angular access to the sample space substantially complicates AD-XRD.³⁶⁻⁴⁰ There is then an obvious commonality with experiments at large-scale laser facilities; angular access at such facilities is strongly constrained by the beam paths of the laser light itself.

AD-XRD from laser-shock compressed, disordered Al has recently been reported by Ma, *et al.*,³⁵ and this first such study illustrates both the scientific benefits and technical drawbacks of AD-XRD for large-scale laser facilities. Specifically, concerning the latter, a few high-resolution spectrometers must be moved between different scattering angles for different shots so as to obtain a complete characterization of $S(k)$ by pooling the results of many shots after suitable normalization or other characterization of shot-to-shot variations in the source or target. While the study of Ma, *et al.*,³⁵ has overcome these challenges and provides an interesting comparison of experiment to modern theoretical treatments of the structure of dense plasmas, it is still important to note that the use of a multi-shot technique has, at a minimum, decreased the range of phase space that can be studied subject to the strong

constraints that exist on facility access. A single-shot alternative could therefore have high scientific impact and is likely the only way that $S(k)$ will be measured on disordered dense plasmas at the National Ignition Facility, where the number of shots per scientific study is especially limited.

Consequently, with the above context established, we report here a photometric analysis of ED-XRD for laser-shock experiments illuminated by broad-band backlighter sources. This analysis makes use of known results for the spectrum of a broad-band backlighter, representative experimental results for $S(k)$ for disordered systems, and representative, established technical characteristics of spectrally-resolving detectors available at large-scale laser facilities. We find significant benefits to ED-XRD for disordered systems, including single-shot determination of $S(k)$, and we propose that ED-XRD should become a standard diagnostic at large-scale facilities such as OMEGA and the National Ignition Facility.

We continue as follows. In section 2 we describe the methods used in the photometric analysis, including the reference target, modeled experimental geometry, and any assumptions about detector or spectrometer performance. In section 3 we present and discuss our results for ED-XRD using each of two different experimental configurations. These are, first, an x-ray CCD detector operating in single-photon mode as an energy-resolving solid-state detector and, second, a wavelength-dispersive spectrometer using a highly-oriented pyrolytic graphite (HOPG) mosaic crystal as the diffractive element. The CCD configuration is viable, but has some drawbacks associated with saturation and double-counting that require special care. We find that the HOPG-based spectrometer quite easily resolves the energy spectrum of the diffraction with excellent counting statistics for a broad-band backlighter that has been fielded at OMEGA, with the caveat that a single HOPG crystal analyzer covers a narrower energy range, and hence a more restricted k -range, than a CCD detector. Finally, in section IV we conclude.

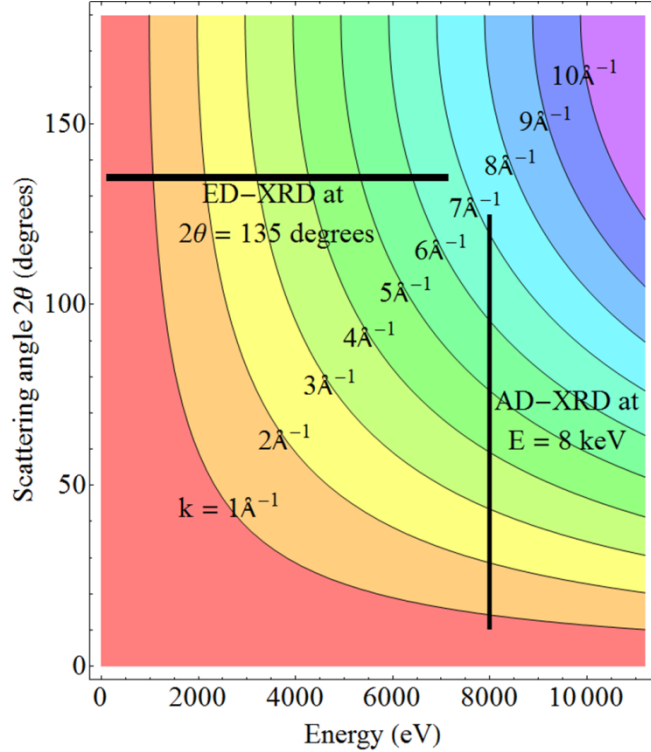
3.2 II Methods

3.2.1 II.A. Source and target

One readily available broadband source in laser shock experiments is the thermal spectrum from a laser-imploded polymer shell, usually filled with H₂-D₂ gas^{41, 42}. In Fig. 3.3 we show a typical spectrum collected at OMEGA⁴³. Because of the spectrum's supra-exponential decay, an ED-XRD experiment with this source is preferentially conducted at low energy, between 2 and 6 keV, as shown in the ED-XRD curve at a scattering angle of 135 degrees in Fig. 3.2.1. Also shown in Fig. 3.3 is the spectrum for a typical narrow band backlighter source at OMEGA, where these sources have seen extensive use in x-ray scattering studies, both elastic (XRD)³⁵ and inelastic (usually called 'x-ray Thomson scattering')²⁵. The narrow-band spectrum is obtained by scaling the spectrum of a Cu *K* target driven by a 10 J, 10 ps laser pulse at the MTW laser facility to a 2.5 kJ, 10 ps laser pulse at OMEGA, using a typical *K* photon yield of $4 \cdot 10^{10}$ photons per J of laser energy^{44, 45}.

We consider two target systems where experimental $S(k)$ are available: liquid boron at ambient pressure and shock-compressed aluminum. For liquid boron we use the experimental results of Krishnan *et al.*^{46, 47}, the data for which were taken at a synchrotron light source using hydrodynamically-levitated boron heated to 2400K by continuous illumination from infrared lasers. While this is not a WDM system *per se*, it is a reasonable surrogate. As shown in Fig. 3.2.1 (a), note the presence of a few broad peaks in $S(k)$, representative of a system with only limited, short-range information in $g_{ii}(r)$. For clarity in our photometric analysis, we will use a smoothed $S(k)$ where the sharp (nonphysical) noise in the experimental $S(k)$ has been filtered. On the other hand, $S(k)$ for shock-compressed aluminum ($n_e = 5.4 \cdot 10^{23} \text{ cm}^{-3}$; $T_e = 10 \text{ eV}$) is based on results from Ma *et al.*³⁵, who have recently reported the first AD-XRD measurement of a shock-compressed, disordered WDM system. $S(k)$ was recovered from Ma *et al.*'s theoretical calculation of an elastic scattering profile for triply-ionized shock-compressed aluminum, to which they fit their data. We note that only an approximate atomic form factor, that of ambient aluminum, was used to calculate $S(k)$ from

Figure 3.1: Contours of equal momentum transfer k (labeled in units of \AA^{-1}) in energy and scattering angle. Angle-dispersive x-ray diffraction (AD-XRD) and energy-dispersive x-ray diffraction (ED-XRD) take vertical and horizontal cuts, respectively, to achieve broad coverage in k and thus obtain information about the radial distribution function.

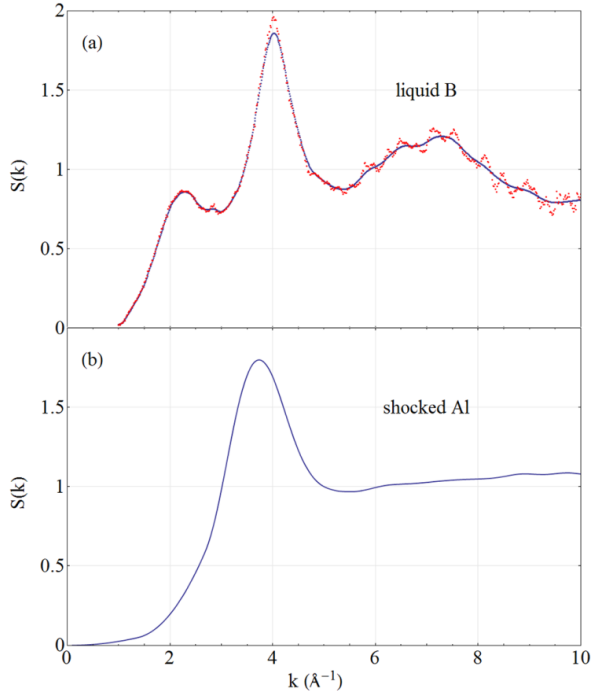


the scattering profile; however, the resulting error in $S(k)$ is expected to be negligible above $k = 3\text{\AA}^{-1}$, and hence does not affect the location of any coordination peaks. As shown in Fig. 3.2.1 (b), note again that the presence of only short-range order in the target results in a simple form for $S(k)$. In this case, the information content is largely limited to the location and intensity of the obvious first coordination peak.

3.2.2 II.B. Photon-electron interactions and numerical modeling

For the targets considered here, the experiment is conducted in an energy region far above any atomic fluorescence from the targets and also far above any soft x-ray blackbody radi-

Figure 3.2: (a): Liquid structure factor of B at 2400K. The original data (red) of Krishnan *et al.*⁴⁶ contains sharp unphysical noise; we therefore use the filtered interpolation (blue) of the data for $S(k)$ throughout this paper. (b): Equivalent theoretical curve for shock-compressed Al at electron density $n_e = 5.4 \cdot 10^{23} \text{ cm}^{-3}$ and temperature $T_e = 10 \text{ eV}$ based on Ma *et al.*³⁵ The curve is based on an approximate treatment of this system’s atomic form factor (see the text for details).



ation from the surface or bulk of the target, each of which is easily attenuated in practice with a thin plastic or Be shield. Consequently, we need only consider the coherent and incoherent scattering of the x-rays as direct contributors to the measured scattering signal; the photoelectric interaction appears only in its contribution to absorption coefficient in the energy range of interest. Note that by coherent here we refer to the quasielastic scattering process itself, *i.e.* “ordinary” diffraction, with no expectation of coherence of the incident beam (such as is used in diffraction experiments at XFEL facilities).

Given a backlighter source with fluence $I_{\text{source}}(E)$ (units of photons/eV, integrated over

4 steradian) at a distance d_{source} from the target, the areal flux incident in the target is $I_{\text{incident}}(E) = I_{\text{source}}(E)/4\pi d_{\text{source}}^2$. The contribution of coherent scattering to the measured energy spectrum at a scattering angle 2θ is then

$$I_{\text{coh}}(E, 2\theta) = I_{\text{incident}}(E) \frac{d\sigma_{\text{coh}}}{d}(k) d\Omega_{\text{det}} \eta_{\text{det}}(E) \tau_{\text{coh}}(E, 2\theta), \quad (3)$$

where k is implicitly determined by E and 2θ , $d\Omega_{\text{det}}$ is the solid angle subtended by the detector, $\eta_{\text{det}}(E)$ is the net efficiency of detection of photons of energy E that arrive in $d\Omega_{\text{det}}$, and $\tau_{\text{coh}}(E, 2\theta)$ includes the necessary corrections to the measured XRD due to the target's geometry and energy-dependent absorption coefficient³⁴. When operating near to a backscattering geometry, for example, $\tau_{\text{sample}}(E, 2\theta) \sim \rho A(1 - e^{-2\mu(E)d})/2\mu(E)$ where ρ is atomic (number) density, A is the cross-sectional area of the portion of the backlighter beam that illuminates the target region of interest, d is the target thickness, and $\mu(E)$ is the x-ray absorption coefficient. For present purposes, $d\sigma_{\text{coh}}/d\Omega$ includes all elastic and quasielastic scattering; it integrates over all ion-ion correlation dynamics⁴⁸.

The incoherent contribution to the measured signal is somewhat more complex to model. The microscopic physics of the incoherent scattering processes, wherein one must address both momentum transfer (k) and energy transfer (ω), results in the need for a double differential cross-section $d^2\sigma_{\text{incoh}} \frac{(k, \omega)}{dd} \Omega$. The detected intensity from incoherent scattering is then

$$I_{\text{incoh}}(E, 2\theta) = d\Omega_{\text{det}} N_{\text{atoms}} \frac{d\sigma_t}{d\Omega} \int_0^\infty dE' I_{\text{incident}}(E') S_{\text{incoh}}(k, \omega) \tau_{\text{incoh}}(E', E, 2\theta) \quad (4),$$

where N_{atoms} is the number of atoms in the target, k is again implicitly determined by E , E' , and 2θ and $\tau_{\text{incoh}}(E', E, 2\theta)$ includes the influence of attenuation for an incident photon of energy E' that scatters through an angle 2θ and departs the incoherent interaction with energy E . In the first Born approximation, $d^2\sigma_{\text{incoh}}/d\omega d\Omega = (d\sigma_t/d\Omega) S_{\text{incoh}}(k, \omega)$, where $d\sigma_t/d\Omega$ is the Thomson differential scattering cross section and $S_{\text{incoh}}(k, \omega)$ is the inelastic component of the dynamic structure factor. In the independent-electron approximation⁴⁹,⁵⁰, $S_{\text{incoh}}(k, \omega)$ may be expressed as a sum over electrons and matrix elements between the initial and final states of the system:

$$S_{\text{incoh}}(k, \omega) = \sum_j \sum_{f \neq i} \left| \langle i | e^{i \mathbf{q} \bullet \mathbf{r}_j} | f \rangle \right|^2 \delta(E_f - E_i - \omega). \quad (5)$$

At sufficiently high k , $S_{\text{incoh}}(k, \omega)$ is peaked at the Compton shift $\Delta E = ^2k^2/2m$. In the high- k (non-collective) scattering regime the total inelastic portion of the dynamic structure factor is constructed using equation (5) evaluated as a sum over individual valence and core electrons. In our modeling procedure this consists of truncated valence and core Compton profiles generated in the impulse approximation^{50, 51} where $S_{\text{incoh}}(k, \omega)$ depends only on the ground state electronic density and kinematics of the scattering process. The first moment of $S_{\text{incoh}}(k, \omega)$ was normalized after truncation according to the Bethe f -sum rule⁵². For boron our approximation yields incoherent scattering cross sections which exceed experimental values by up to 30 percent, making our approximate treatment of the incoherent background conservative. In the relevant range of momentum transfers the Compton shift is sufficiently small that we substitute $\tau_{\text{coh}}(E, 2\theta)$ for $\tau_{\text{incoh}}(E, E', 2\theta)$ without introducing appreciable systematic error, allowing τ to be factored out of the integrand in equation (4). Similarly, the FWHM of $S_{\text{incoh}}(k, \omega)$ (which, in the impulse approximation, is directly related to the width of the momentum distribution of the electronic ground state) is small compared to our required energy resolution, such that we can define a Compton-shifted energy variable $E^* = E + \Delta E$ and re-express (4) in approximate form:

$$I_{\text{incoh}}(E, 2\theta) = d\Omega_{\text{det}} N_{\text{atoms}} \frac{d\sigma_t}{d\Omega} \tau_{\text{coh}}(E, 2\theta) I_{\text{incident}}(E^*) \int_0^\infty dE' S_{\text{incoh}}(k, \omega). \quad (6)$$

The total scattered intensity, in units of photons/sr, is then

$$\begin{aligned} I_{\text{total}}(E) &= d\Omega_t N_{\text{atoms}} \tau(E, 2\theta) \frac{d\sigma_t}{d\Omega} [I_{\text{incident}}(E) f(k)^2 S(k) + \\ &\quad I_{\text{incident}}(E) \int_0^\infty dE' S_{\text{incoh}}(k, \omega)]. \end{aligned} \quad (3.1)$$

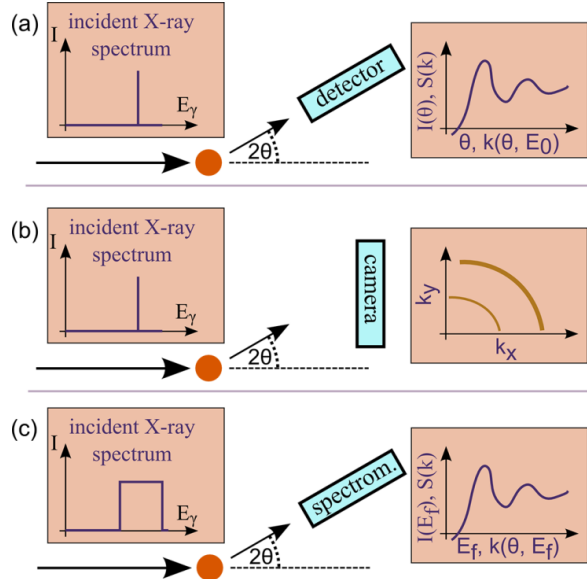
Note that $\int_0^\infty dE' S_{\text{incoh}}(k, \omega) = N$ (the atomic number of the scattering species) in the high- k limit of the impulse approximation⁵¹ and takes on smaller values at lower momentum transfers; by comparison, $f(0)^2 = N^2$, and $S(k)$ is of order unity. Therefore the first (coherent) term in $I_{\text{total}}(E)$ dominates for heavier elements or for sufficiently small momentum transfers. In Fig. 3.3 (a) and (b) we compare $f(k)^2$ to the incoherent background scattering for the above-described model. These results lead us to expect that the background in an

ED-XRD experiment will not substantially limit the ability to observe the desired coherent scattering.

3.2.3 II.C. Spectrometers for detection of ED-XRD

We now consider two different detection options. As shown in the schematic of Fig. 3.2.3, one or both of an x-ray CCD and a HOPG-based spectrometer may be used as energy-sensitive detectors. Simulated spectra for both follow in section III. Throughout the remainder of the paper the following experimental parameters are used: $d_{\text{source}} = 1 \text{ cm}$; target dimensions (for both B and Al): 0.25 mm 0.25 mm 0.1 mm; scattering angle $2\theta = 135$ degrees. These choices will be motivated below.

Figure 3.3: Schematic representations of (a) and (b) angle-dispersive x-ray diffraction, compared to (c) energy-dispersive x-ray diffraction (ED-XRD).



The modeled CCD has a 2-dimensional square grid of 2200 x 2200 pixels, with a pixel edge length of 13.5 microns. A quantum efficiency of 1 is assumed. The optimal distance between the detector and the target is determined by the competing demands of high signal collection and high rejection of two-photon events on single pixels. We find it reasonable to

balance these demands by selecting a single photon-hit regime with an expectation value p of 0.1 photon hits per pixel. At a given scattering angle and in the absence of addition of any special absorbers between the target and the CCD other than a Be filter for low-energy photon rejection, p is determined by the working distance of the CCD and the scattered intensity off the target. The working distance is not a highly-constrained parameter; it must merely be sufficiently large that backgrounds from the high neutron flux and other stray radiations are likely to be substantially suppressed. An upper bound on target intensity arises from signal broadening due to the finite angular size subtended by the target relative to the backlighter. We require this geometrical broadening in momentum transfer, k , to satisfy $\Delta k/k < 0.05$, such that it is sufficiently small compared to the intrinsic scale of structure in $S(k)$. We label the angle subtended by the target $\Delta\theta_t$ and express the geometrical broadening in terms of it: $\Delta k/k = \cot \theta_t$. At $2\theta = 135$ degrees the maximal $\Delta\theta_t$ is approximately 0.1 radians, which corresponds to a sample length of 1 mm.

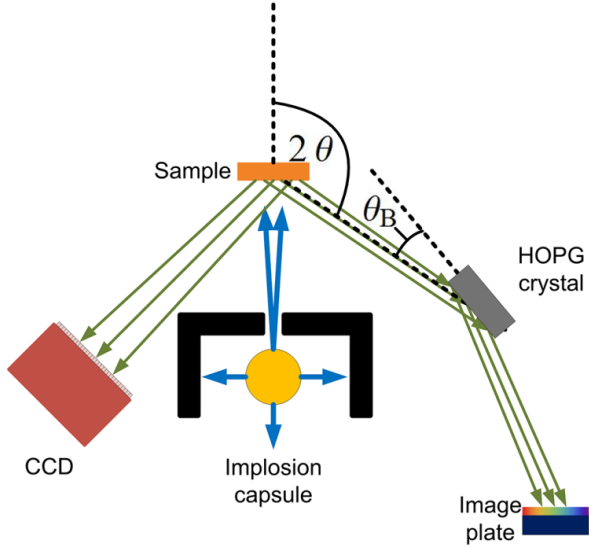
The task of presenting a modeled HOPG spectrum in a non-configuration-specific manner is complicated by the significant dependence of the spectrometer's energy range on several geometric parameters. Using the labeling of Fig. 3.2.3 and, as an example, the spectrometer geometry described by Fig. 3.2.3 (a), the differential in k for scattering from the target is

$$dk = \frac{k}{E} dE + \frac{k}{\delta(2\theta)} d(2\theta) = \frac{E}{c} (\sin(\theta) \cot \theta_B - \cos(\theta)) d\theta. \quad (9)$$

As a crystal of length l located a distance F from the target subtends an angle of approximately $(l/F) \sin \theta_B$, we can directly use (9) to calculate the range k covered by an analyzer crystal as a function of k , 2θ , and the choice of HOPG reflection. Fig. 3.2.3 illustrates this. Salient features of $\Delta k(k, 2\theta)$ are that it is asymptotically linear in k and depends weakly on 2θ everywhere except at low k .

That said, we can choose a typical configuration for an HOPG spectrometer and generate a detected spectrum that spans the entire range of k with which we are concerned. Conceptually, this is done by repeatedly rotating the crystal to different central θ_B to acquire narrow spectra in different ranges of k and then stitching together the resulting spectra. This spectrum, which is henceforth referred to as the "HOPG source spectrum", does not

Figure 3.4: Experimental configuration for ED-XRD at a laser shock facility. A long pulse-driven CH capsule emits a broad thermal spectrum. Scattering from the target is observed using an HOPG spectrometer or a CCD in the single-photon hit regime.



represent a realistic data set, since acquiring it in a single shot would require prohibitively many analyzer crystals, but it does serve as a convenient compilation of the ensemble of possible experimental configurations; the exact choice of spectrometer configuration for a given experiment depends on some prior knowledge of the desired k range, as we discuss below.

The modeled HOPG spectrometer is qualitatively similar to several instruments that have previously been fielded for x-ray Thomson scattering studies at OMEGA⁵³⁻⁵⁵. For our modeled instrument, the HOPG diffractive element operates on the 002 reflection, has a mosaic spread of 0.3 degrees, is taken to be a flat square with side length $l = 12$ cm, and is located at a distance $F = 25$ cm from the target. The energy-dependent integral reflectivity of the HOPG is based on computed reflectivity curves⁵⁶ for an HOPG crystal having a mosaic spread of 0.3 degrees. Denoting r as the peak reflectivity and ω as the FWHM of the reflectivity curve, the angular integral reflectivity, $\Delta\theta_B$, is approximately r ; equivalently,

the integral reflectivity in energy units is $\Delta E = E \cot \theta_B \Delta \theta_B$. We define E_{\max} and E_{\min} as the maximum and minimum energies diffracted by the crystal. For isotropically-scattered photons with a fixed energy E between E_{\max} and E_{\min} the probability of reflection is $\eta = \Omega_0 \Delta E / (4 \pi (E_{\max} - E_{\min}))$, where $\Omega_0 = (l/F)^2 \sin \theta_B$ is the solid angle subtended by the crystal relative to the source (units of sr). Correspondingly, the detected spectrum resulting from I_{incident} on the target is $I_d(E) = 4\pi \eta dI_{\text{incident}}(E) / d\Omega = \Delta \theta_B (l/F) dI_{\text{incident}}(E) / d\Omega$. For reference, $\Delta \theta_B l / F = 7 \times 10^{-4}$ at 4 keV. It will be seen in the next section that the resulting net collection efficiency in a given achievable energy band is several orders of magnitude higher than that of the CCD.

3.3 III Results and discussion

There is good reason to believe, heuristically, that the above-described experimental configurations for ED-XRD should determine $S(k)$ with adequate statistics. Numerous past x-ray Thomson scattering experiments at laser plasma facilities have measured the inelastic portion of $S(k, \omega)$ using narrow pulse backlighters for illumination^{25, 27, 28, 57-60}. Above 2 keV, a broad-band thermal backlighter has approximately 100 times the photon conversion efficiency of a short-pulse Cu K backlighter (Fig. 3.3); additionally, the elastic scattering cross section is typically larger than the Compton cross section, as discussed in section II and shown in Fig. 3.3 (a) and 5 (b). Thus, ED-XRD should offer vastly higher signal intensity than (quasi-monochromatic) x-ray Thomson scattering using a metal-foil backlighter, and therefore better statistics.

Figure 3.5: Range k in momentum transfer of scattering off the target probed by a small HOPG crystal per degree of its maximum subtended angle, θ_{\max} , for three spectrometer geometries that involve the same position (but different rotations) of the HOPG crystal: (a) the detector located in the target scattering plane and away from the axis passing through the backlighter and target, (b) the detector located in the target scattering plane and near the axis passing through the backlighter and target, and (c) the detector located such that it, the target, and the HOPG crystal define a plane perpendicular to the scattering plane. θ_{\max} denotes the maximum possible subtended angle of the HOPG crystal given a fixed spectrometer working distance F ; *i.e.*, for a crystal of length l , the maximum subtended angle is $\theta_{\max} = l/F$.

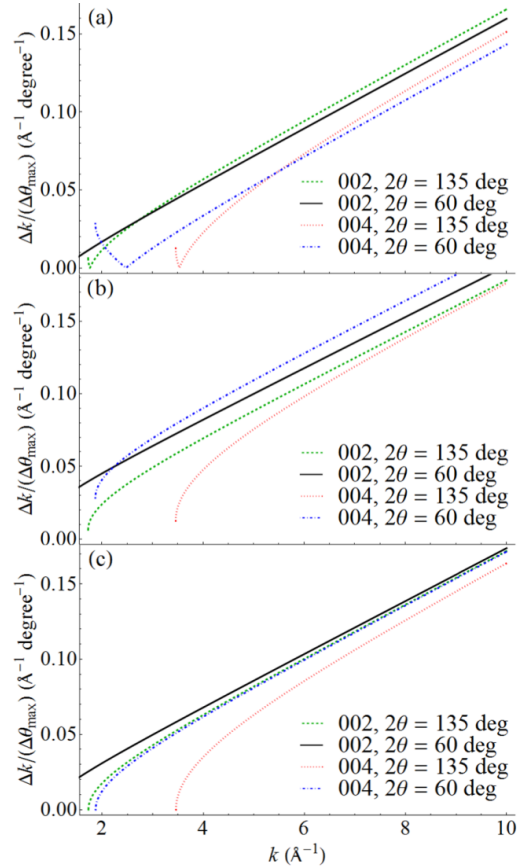


Figure 3.6: Elastic and inelastic contributions to the differential cross section of (a) boron and (b) aluminum. The elastic cross sections are based on tabulated values of $f(k)$. The inelastic differential cross sections, defined by $N_{\text{incoh}}(k) = \int_0^\infty dE' S(k, \omega')$, are based on $S(k, \omega')$ generated from f -summed, truncated Compton profiles in the impulse approximation. See the text for further details.

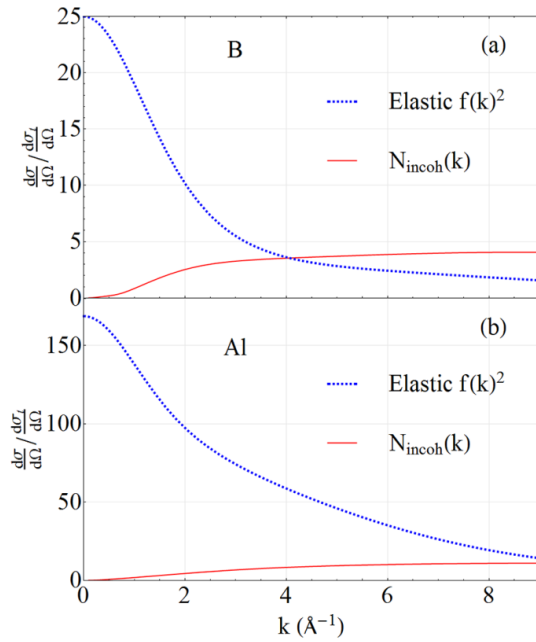
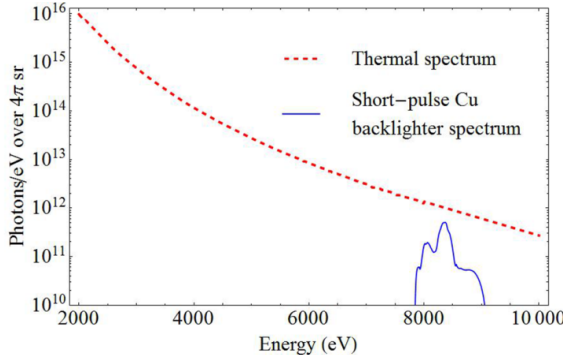


Figure 3.7: Red: experimental thermal backlighter spectrum from OMEGA ⁴³. Blue: a short-pulse Cu K backlighter spectrum, based on scaling of results from a lower energy laser system to a 2.5 kJ, 10 ps laser shot at OMEGA ^{44, 45}.



In Fig. 3.3 we present $I_d(E)$ defined in section II, filtered by a 20 m Be foil (to reject low-energy photons) for liquid boron acquired on a CCD alongside the equivalent HOPG source spectrum. The highlighted region of the HOPG source spectrum shows the energy range covered by a specific configuration: a 12-cm long HOPG crystal at distance $F = 25$ cm from the target, oriented such that the detected spectrum is centered on the main correlation peak in $S(k)$. This crystal size results in a solid angle subtended by the crystal similar to that in existing high-efficiency HOPG spectrometers ^{43, 61}. Figure 3.3 shows the CCD and HOPG spectra for shock-compressed Al in this same format. $S(k)$ reconstructed for B and Al is presented in Figs. 3.3 and 11, respectively. In both these figures the k -range probed by the specific spectrometer configuration is highlighted. All reconstructed $S(k)$ curves, including those without background subtraction, show a well-defined correlation peak. Note that the uncorrected curves overshoot the experimental $S(k)$ at large k ; this is a result of the monotonically-increasing Compton background (as well as double-counts, for the CCD). This background decreases relative to the XRD signal for larger atomic numbers, as seen by comparison of Figs. 3.3 and 11. The HOPG source spectrum exhibits excellent statistics (error bars < 2 percent) relative to the CCD over the entire plotted energy range. While deteriorating at high energy, the CCD spectrum also has good statistics (error bars < 5

percent) below 4.5 keV.

The relative merits of the two detectors are dictated by particular features of the ED-XRD configuration and the spectrum probed. Despite the substantially better energy resolution of an HOPG spectrometer compared to a Fano-noise limited CCD, energy resolution is a poor criterion for comparison: at 135 degrees scattering angle, the k -width of features in $S(k)$ corresponds to a width in energy greater than 500 eV, substantially larger than the resolution of both the CCD and the HOPG spectrometer. Instead, the leading limitation on data quality is shot noise at high k due to the sharp decay of the source spectrum intensity with increasing energy.

The latter limitation is severe only for the CCD, (1) because of vastly lower overall counts and especially (2) because the intense low-energy portion of the incident spectrum is ‘echoed’ as double-counts at higher energy. In simulated CCD spectra the double-count contribution to the detected spectrum outweighed the single-count contribution above 5 keV. This double-count noise cannot be reduced by varying p : in the single photon-hit regime, the number of double-hits on single pixels scales as p^2 ; the associated Poisson noise scales as p . Single photon counts also scale as p ; as a result, above 5 keV varying p has little effect on the signal-to-noise (*i.e.* single-to-double-count) ratio. It is instead highly preferable to carry out an ED-XRD experiment in near-backscatter geometry, such that the range of k in which $S(k)$ has structure is probed by a lower-energy region of the backscatter spectrum. In fact, the only means of significantly improving data quality on a single hit CCD are (1) using a detector with more pixels to improve statistics, and (2) moving the detector closer to backscatter.

The two spectrometer types offer a variety of configurations adapted to experimental situations in which different k -ranges need to be probed. If the goal is to locate the main correlation peak in $S(k)$, a single-HOPG crystal spectrometer is a viable option (illustrated, as mentioned above, in Figs. 3.3 and 3.3). On the other hand, if the scientific goal requires a significantly wider k -range, then a CCD detector in single photon counting mode, multiple HOPG analyzer crystals, or both are necessary. Despite the CCD’s relatively poor signal to

noise ratio, there is substantial motivation for performing ED-XRD using both spectrometer types if the full k range is desired. In such a dual configuration the CCD would provide low-noise data up to approximately 4.5 keV with one or more HOPG spectrometers covering the remainder of the energy spectrum, corresponding to a reduced range of θ_B from 21 to 49 degrees, for which a modest number of analyzer crystals would be required.

The above results establish single-shot ED-XRD as a viable method for use at OMEGA, even for systems with only liquid-like, isotropic short-range order; this observation clearly extends to fine, isotropic polycrystalline systems where the structure in $S(k)$ can only be sharper. We note that pump laser energy is 30 times larger at NIF than at OMEGA and that the ratio of backlighter fluences exceeds that factor due to the higher backlighter electron temperature at NIF⁴¹. Consequently, ED-XRD is also viable at NIF where the higher backlighter fluence may allow a substantial reduction in solid angle subtended by an HOPG spectrometer, compared to present calculations. This would in turn allow incorporating a larger number of spectrometers in a single diagnostic module. CCD-based studies at NIF are also, in principle, viable but may run into technical difficulties related to neutron backgrounds or difficulty in shielding from electromagnetic pulses.

Figure 3.8: Photon-energy histograms on CCD and HOPG spectrometers for shock-compressed Al at electron density $n_e = 5.4 \cdot 10^{23} \text{ cm}^{-3}$ and temperature $T_e = 10 \text{ eV}$, using Ma *et al.*'s best-fitting theoretical model to their experimental results for $f(k)^2 S(k)$ ³⁵, and assuming $f(k)$ of ambient Al. The expectation value of photon counts/pixel on the CCD is $p = 0.1$. The energy range of a specific HOPG configuration using a 12-cm long HOPG analyzer is denoted by the shaded region, the width of which corresponds to the spectrometer configuration of Fig. 7 (a). The spectrometer's focal length is 25 cm, and the length of the crystal in the non-energy dispersive orientation is 12 cm; both spectrometers are positioned at $2\theta = 135$ deg. A 20-m thick Be foil is used to reject low-energy photons. Error bars in the HOPG histogram are smaller than 1% (not shown).

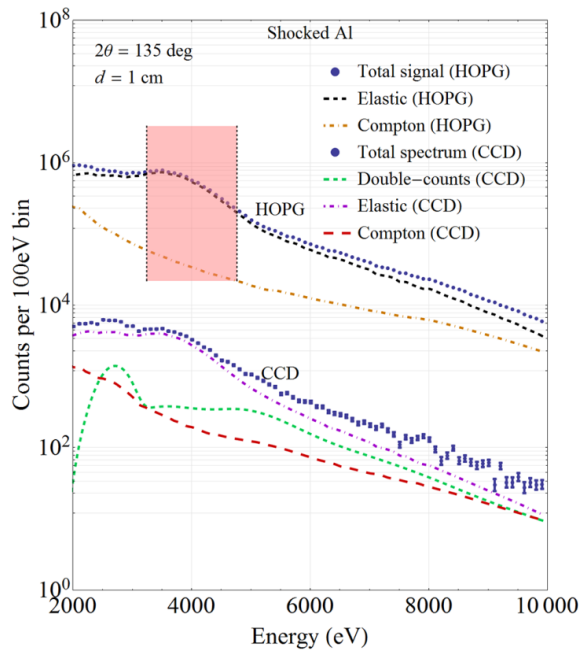


Figure 3.9: Photon-energy histograms for energy-dispersive diffraction spectra of liquid boron on CCD and HOPG spectrometers. The expectation value of photon counts/pixel on the CCD is $p = 0.1$. The energy range of a specific HOPG configuration using a 12-cm long HOPG analyzer is denoted by the shaded region, the width of which corresponds to the spectrometer configuration of Fig. 7 (a). The spectrometer’s focal length is 25 cm, and the length of the crystal in the non-energy dispersive orientation is 12 cm; both spectrometers are positioned at $2\theta = 135$ deg. A 20-m thick Be foil is used to reject low-energy photons. Error bars in the HOPG histogram are smaller than the size of the symbols.

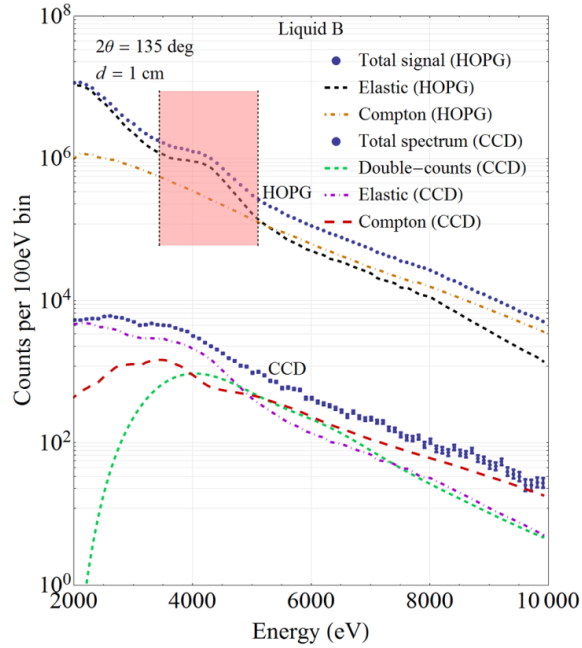


Figure 3.10: $S(k)$ for liquid boron reconstructed from simulated energy-dispersive spectra of Fig. 8 for (a) an HOPG spectrometer and (b) a CCD, with and without subtraction of Compton background and photon double-counts. Data bin size is 100 eV. The shaded k -range in the HOPG spectrum corresponds to the spectrometer configuration described in the text, and is centered about the main correlation peak in $S(k)$.

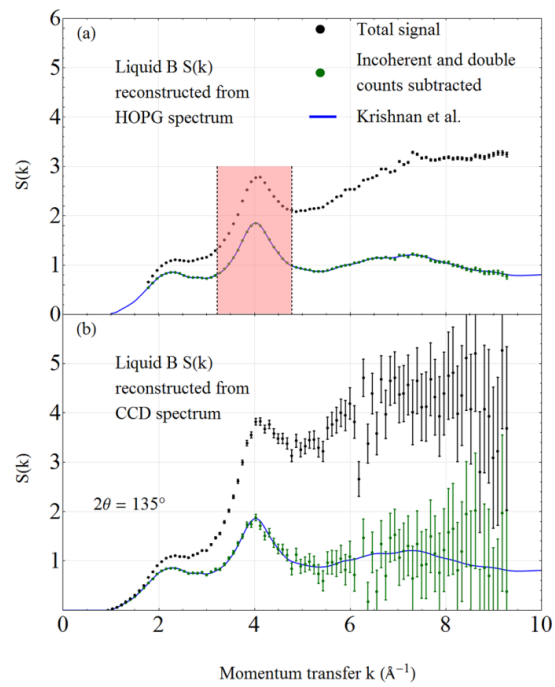
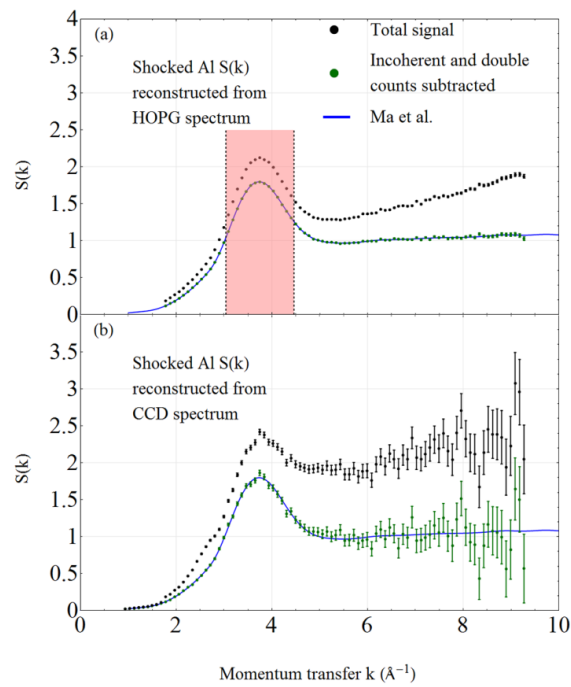


Figure 3.11: In blue: X-ray structure factor $S(k)$ for shock-compressed Al computed from Ma, *et al.*³⁵. Overlaid with $S(k)$ reconstructed from the spectra of Fig. 9 for (a) an HOPG spectrometer and (b) a CCD. The data bin size is 100 eV. The shaded k -range in the HOPG spectrum corresponds to the spectrometer configuration described in the text and is centered about the main correlation peak in $S(k)$.



3.4 IV. Conclusions

We report a photometric study of the viability of single-shot investigation of the isotropic static structure factor $S(k)$ in experiments using a broadband x-ray backlighter as the source for energy-dispersive x-ray diffraction (ED-XRD). The results are extremely favorable, and indicate that single-shot ED-XRD can be used at OMEGA or NIF. A standard scientific-grade x-ray CCD camera operating in single-photon counting mode suffices for many studies, but exhibits degraded performance at high momentum transfers due to the rapid decrease of incident flux at higher photon energy. On the other hand, a typical HOPG-based wavelength dispersive spectrometer has exceptional count rates in any selected k range, but its limited energy range may require either the use of multiple spectrometers or of a single compound spectrometer having multiple analyzer crystals.

3.5 Acknowledgements

We thank Brian Mattern, Tilo Doeppner, Philip Nilson, Barukh Yaakobi, Christian Stoeckl, Yuan Ping, Justin Wark, and Andrew Higginbotham for helpful discussions. This work was supported by the US Department of Energy, Office of Science, Fusion Energy Sciences and the National Nuclear Security Administration, through grant DE-SC0008580.

3.6 References

- 3.6.1 ¹ J. D. Lindl, P. Amendt, R. L. Berger, S. G. Glendinning, S. H. Glenzer, S. W. Haan, R. L. Kauffman, O. L. Landen, and L. J. Suter, *Physics of Plasmas* 11, 339 (2004).
- 3.6.2 ² E. I. Moses, *Nuclear Fusion* 49, 104022 (2009).
- 3.6.3 ³ F. Langenhorst, M. Boustie, A. Migault, and J. P. Romain, *Earth and Planetary Science Letters* 173, 333 (1999).
- 3.6.4 ⁴ J. Gattacceca, M. Boustie, E. Lima, B. P. Weiss, T. de Reseguier, and J. P. Cuq-Lelandais, *Physics of the Earth and Planetary Interiors* 182, 42 (2010).
- 3.6.5 ⁵ H. Takabe, et al., *Plasma Physics and Controlled Fusion* 50, 124057 (2008).
- 3.6.6 ⁶ L. O. Silva, M. Marti, J. R. Davies, R. A. Fonseca, C. Ren, F. S. Tsung, and W. B. Mori, *Physical Review Letters* 92, 015002 (2004).
- 3.6.7 ⁷ B. A. Remington, R. P. Drake, H. Takabe, and D. Arnett, *Physics of Plasmas* 7, 1641 (2000).
- 3.6.8 ⁸ H.-S. Park, et al., *High Energy Density Physics* 8, 38 (2012).
- 3.6.9 ⁹ M. Koenig, et al., *Physics of Plasmas* 13, 056504 (2006).
- 3.6.10 ¹⁰ A. Macchi, M. Borghesi, and M. Passoni, *Reviews of Modern Physics* 85, 751 (2013).
- 3.6.11 ¹¹ G. Gregori, et al., *Nature* 481, 480 (2012).
- 3.6.12 ¹² F. Fiuzza, R. A. Fonseca, J. Tonge, W. B. Mori, and L. O. Silva, *Physical Review Letters* 108, 235004 (2012).
- 3.6.13 ¹³ F. Dollar, et al., *Physical Review Letters* 110, 175002 (2013).
- 3.6.14 ¹⁴ K. U. Akli, et al., *Physical Review Letters* 100, 165002 (2008).
- 3.6.15 ¹⁵ B. K. F. Young, et al., *Review of Scientific Instruments* 69, 4049 (1998).
- 3.6.16 ¹⁶ K. Oades, A. Evans, G. Slark, J. Foster, R. Eagleton, and E. Clark, *Review of*

Chapter 4

X-RAY FREE ELECTRON LASER-BASED STUDIES OF WDM

4.1 X-ray Free Electron Lasers

XFELs produce radiation of unprecedented brilliance (10 orders of magnitude higher than undulator radiation from third-generation synchrotron sources), full transverse coherence, pulse durations as short as 10 fs. This combination of capability far exceeds that possible with third-generation light sources and opens new frontiers in imaging and the interrogation of ultrafast processes in materials science and biology (cites). In this section we give an overview of the technology and its range of applications in the study of HED states of matter.

4.1.1 Physics of XFELs

To describe the FEL interaction, we first consider the generic case of radiation emission from undulators, the type of insertion device used in both XFELs and the highest-brilliance beamlines at third-generation synchrotron light sources.

A simple time-of-flight argument may be used to obtain an intuitve understanding of radiation by a single electron in an undulator. A radiation wavefront co-propagating with an electron undergoing forced transverse undultion with a (longitudinal) period λ_u will move ahead of the electron. Constructive interference of the radiation field produced by successive undulationso of the electron will occur at discrete values of the electromagnetic wavelength, λ_n , satisfying $\lambda_n = \lambda_1/n$, where λ_1 is defined as the fundamental resonant wavelength. The time t taken for an electron to propagate one undulator period λ_u at speed v_z ($t = \lambda_u/v_z$) is equal to that needed for a resonant wavefront travel the distance $\lambda_u + n\lambda_n$. Equating the propagation times for the wavefront and electron yields the relation (cite McNeil et al.)

$$\lambda_n = \frac{\lambda_u}{n} \left(\frac{1 - v_z/c}{v_z/c} \right). \quad (4.1)$$

More detailed treatment shows that, in the case of a helical undulator, only the fundamental mode has strong on-axis emission. (cites)

This describes the narrow spectral width of undulator radiation and the coherent addition of radiated wave amplitudes by a single electron over the length of an undulator. This constructive interference accounts for the much higher brilliance of radiation produced by an undulator, compared to a wiggler or bending magnet.

At a synchrotron light source electrons in a bunch have uncorrelated positions, and the undulator spectrum is therefore a simple incoherent sum of the emission of all individual electrons passing through it. An XFEL improves on this by creating a positional ordering electrons into ‘micro-bunches’ separated from one another by the radiation field wavelength. The coherent emission from multiple micro-bunches with N_b electrons each would be equivalent, in an idealized case where the micro-bunch dimension were much smaller than the x-ray wavelength, to that from point-like charges of magnitude eN_b , with a resulting factor of N_b^2 enhancement in brilliance relative to that from an incoherently-emmitting electron bunch. (cite)

Electrons in an undulator experience a longitudinal force from the radiation field that is modulated by its period. The consequent bunching of electrons with a period equal to the X-ray wavelength is a self-reinforcing process referred to as self amplified stimulated emission (SASE) (cites). Crucially, the occurrence of SASE requires a sufficiently strong initial radiation field, which third-generation synchrotron storage rings—having 100 ps-duration electron bunches—are not capable of producing. The key feature of an XFEL is its use of a linear accelerator to produce very compact electron bunches with sufficient electron density to bootstrap SASE.

4.1.2 XFELs and WDM generation

Maximum single-shot flux densities available at XFELs exceed 10^4 J/cm^2 , sufficient to produce HED states with per atom energy deposition over 100 eV with uniform, volumetric heating. (TODO: how about better-focusing optics?). Because XFEL radiation is monochromatic it can be used as a probe for nearly all X-ray diagnostics useful for determination of the state variables of WDM, with the notable exception of XAS. Taken together, these characteristics make XFELs ideal for both producing and probing short-timescale dynamics of HED matter. (cites)

One of the most significant recent advances in XFEL technology is the generation of two-color pairs of hard X-ray pulses. This is done by production of time-delayed twin electron bunches (achieved either by illuminating the source cathode with a train of two laser pulses, or using an emittance spoiler) (cite Marinelli et al., Lutman et al.) and the addition of magnetic chicanes that introduce a time-energy correlation in the electron beam before the bunches' entry into the undulator. At the LCLS, two color X-ray pulse energies up to the mJ level—approaching the values of single-pulse SASE—have been demonstrated. X-ray arrival time delays are variable between 30 and 125 fs, and maximum color separations of up to 1.9 % of the photon energy have been demonstrated (cite Lutman).

Operating an XFEL in two-color mode opens up significant possibilities for truly time-resolved probes of WDM. In single-pulse operation the time evolution of an XFEL-heated target can, to some extent, be studied by variation of pulse duration. However, such a study yields a signal that, for each XFEL configuration, is a convolution over all states the target transitioned as it heated throughout each pulse's duration. In contrast, two-color operation offers two advantages:

- Temporal resolution: by choosing pulse energies that straddle an absorption edge of a chemical filter (in the case of an XRD probe), or of the target itself (in the case of an XES probe), signal from the pump pulse can be rejected. Varying pump-probe delay thus allows measuring the sample's temporal response to the pump.

- Uniformity of probed state: By additionally reducing the intensity of the probe relative to the pump, one can ensure that the probe is only a weak perturbation to the heated state generated by the pump.

The possibility of clean time-resolved studies of XFEL-generated WDM is quite attractive, given that the electronic relaxation cascade in a heated solid consists of several partially-overlapping stages of uncertain durations: i.e. collisional ionization by hot electrons; stimulation of long-wavelength collective excitations; and damping of large-q excitations through production of electron-hole pairs. Lack of prior information in the physics under scrutiny emphasizes the need for the highest-information diagnostics available.

4.2 HED physics at XFEL facilities

4.2.1 Early experiments

Initial efforts at FLASH and LCLS, the first free electron lasers operating at short wavelengths, have been focused on the creation of exotic states and the exploration of interactions of high-intensity hard X rays with matter. Thomas et al. and others have studied the Coulomb explosion of noble gas clusters, including the dynamics of nanoplasma formation (cite Thomas et al.). Using intense XFEL radiation Young et al. demonstrated the production of fully-stripped Ne atoms as well as induced X-ray transparency in ‘hollow’ atoms, a manifestation of ‘beating’ the Auger clock though ionization rates faster than the recombination times of core electrons. Their modeling of X-ray/atom interactions using a rate-equation based approach yielded predictions of atomic populations consistent with electron spectroscopy, providing an early validation of the applicaton of population kinetics codes such as SCFLY to the simulation of XFEL-matter interactions. (cite Young, maybe cite SCFLY paper and check that it wasn’t originally written with XFEL simulation in mind).

Nagler et al. have similarly demonstrated saturable absorption of an L-shell transition in Al, where the long lifetime of 2p vacancies allowed complete depopulation within a single XFEL pulse at incident intensities on the order of 10^{16} W/cm² and 92 eV photon energy.

(cite Nagler). This experiment was the first demonstration of a bulk, crystalline material in a high-energy density (and highly non-thermal) electronic configuration. (check that this is true).

4.3 Scientific Directions

4.3.1 Time dynamics of WDM states

The ability of XFELs to produce such transient HED states invites basic questions about the creation of these states and their temporal evolution. Population kinetics codes such as SCFLY are a well-established tool to simulate the electronic evolution of an XFEL-heated material, but such codes are based on atomic physics treatments and cannot be all-encompassing, as they omit solid-state electronic structure as well as the interaction of electrons with the lattice of a solid-density system. Hau Riege et al. have examined electron-ion dynamics during heating by a single XFEL pulse, using comparison of Bragg diffraction from heated graphite with molecular dynamics simulation to quantify perturbation of the atomic lattice. They have identified melting of the graphite lattice within 40 fs pulses—far shorter in duration than the ps-timescale of electron-phonon coupling indicating an ultrafast phase transition. We revisit Hau-Riege’s conclusions in a different light in section (which section?), but their work pertinently demonstrates that the characterization of even coarse-grained quantities such as lattice thermalization timescales gives insight into the new physical regimes that XFELs are capable of producing and probing.

Similar observations apply to electron-electron thermalization in a solid, where damped collective excitations (ie. plasmons) may play a significant role as a bottleneck stage between absorption of XFEL photons and eventual thermalization of atomic electrons (cite Egerton, Sorini, maybe dig up cites from HEF paper).

As alluded to above, two-color XFEL operation is a promising potential means of addressing these questions.

4.3.2 Tests of Finite- T electronic structure

The output quantity of a density functional theory (DFT) simulation is real-space charge density. At the same time, the real-space charge distribution of a crystalline XFEL target material can be interrogated via X-ray diffraction, which samples the unit cell structure factor at momentum transfers corresponding to vectors of the reciprocal lattice. Because a material's lattice typically does not have sufficient time to respond to the changing electronic configuration over the duration of an XFEL pulse, XRD from WDM states produced by an XFEL can be directly compared to predictions of frozen-lattice finite-temperature DFT calculations.

This observation has led Valenza et al. to generate predictions of the consequences of XFEL heating on the intensities of Bragg peaks in several materials using DFT calculations in VASP (cite Valenza et al.). They have shown that the information in the XRD signal is sufficient for discrimination between competing theoretical predictions, provided the XRD measurement is performed over a sufficiently wide range of momentum transfers. Valenza et al. demonstrate strong testable signatures of condensed-phase effects in each of LiF, graphite, diamond, and Be as a result of heating to temperatures on the order of 10 eV. A summary of their results is reproduced in Fig. ??.

The capability to test predictions of finite-temperature electronic structure models is a unique feature of XFEL-based experiments. We will explore the topic in some more detail in section (reference section), where we have the opportunity to apply it to experimental data.

4.4 Design of an XFEL heating experiment

One can identify several experimental desirata shared by the majority of XFEL-based studies of WDM wherein the primary probe is X-ray diffraction:

- Maximization of information in the XRD signal
- Effective target heating so as to maximize the accessible range of energy densities

- Time resolution

Each of these can be achieved in one or more ways. Respectively:

- As alluded to in section (reference section), better-constrained estimates of real space charge density can be obtained by sampling a larger number of Bragg reflections. This requires probing a large momentum transfer range, made possible by using a high incident photon energy.
- In bulk samples, a high density of deposited energy requires matching the incident photon energy to a value at which the photoelectric absorption cross section is large. In section (reference section) we will introduce an alternate approach based on the design of structured targets that relaxes this constraint on incident photon energy.
- Wherever a single XFEL pulse is used to both heat and probe a sample, a limited degree of sensitivity to the time-evolution of transient states can be had by varying time duration. Two-color XFEL operation, however, is much more attractive. However, it suffers from tradeoffs: most notably experimental complexity and reduced signal, due to the need for attenuation of the probe pulse relative to the pump.

These goals, and the tradeoffs that accompany them, are important context for both the experimental work described in the next section and the modeling-based exploration of experimental technique discussed in section (reference section).

4.5 Experimental Work

In the following I describe several experimental results arising from two beam runs at the Matter of Extreme Conditions (MEC) endstation at the Linac Coherent Light Source (LCLS) in June of 2014 and January of 2016. The studies conducted addressed questions about the relative magnitudes, and time scales, of lattice and electronic heating in various solids, mainly

metal oxides. The primary diagnostic was XRD, with which we measured changes in electronic charge distribution as a function of incident flux, with the eventual goal of comparison to finite-T condensed matter electronic structure theory, as described in (reference section). The secondary diagnostic—used in a subset of the studies—was a von Hamos X-ray emission spectrometer with a highly annealed pyrolytic graphite (HAPG) analyzer crystal and 9 eV energy resolution, with which heating-induced line shifts and changes in valence-level emission were measured.

Throughout these measurements the XFEL beam was brought to a focus at the sample location using a stack of Be lenses. Flux incident on-sample was altered through a combination of beam attenuation and variation of the focal spot diameter between minimum and maximum values of 2 and 58 microns. XRD data was collected on a quad CSPAD solid state detector downstream from the sample (cite CSPAD paper).

In samples wherein the signal was weak compared to time variations in the area detector pedestal values, additional processing was performed in order to reconstruct signal incident on the detector. This is described in more detail in section (reference section), which details analysis and modeling of electronic heating based on an XRD dataset of XFEL-heated MgO.

4.5.1 Testing Lattice Thermalization in XFEL-heated Solid State Systems

Fig. 4.4 (a, b) displays the progression of Bragg peak intensities as a function of incident flux for two different Fe_3O_4 targets heated by 45 fs XFEL pulses. It demonstrates monotonic declines in the intensities of all Bragg peaks as a function of flux density, with the exception of the 222 peak, which rises to a maximum at the second-lowest flux density point before declining.

It is straightforward to evaluate the relative contributions of thermalization of electronic and lattice degrees of freedom to the XRD signal’s evolution as a function of heating. The main distinguishing feature between these two components is that the latter causes Debye-Waller quenching of Bragg peak intensities that is approximately proportional to $e^{-q^2\langle u^2 \rangle}$, where q is momentum transfer and u is atomic displacement. Fig. 4.5 compares the experi-

mental data to this Debye-Waller progression for several different values of RMS atomic displacement. The experimental data shows a complete lack of Debye-Waller-like q -dependence in Bragg peak intensities at high levels of heating, signifying that the XRD response is strongly dominated by reorganization of electronic charge density within a unit cell.

The electronic response of Fe_3O_4 to XFEL heating can be further interpreted through comparison of the data to a simple atomic form factor-based model of ionization (the model is described more specifically in section (reference section)). We find that the model reproduces the anomalous rise in intensity of the 222 reflection (reference figure) via a loss of destructive interference between the valence wavefunctions of O and Fe as both are simultaneously ionized. (cite paper in preparation).

4.5.2 Observation of Nonlocal Heat Transport in Nanophase Fe_3O_4

4.5.3 XES Signatures of Valence Electron Delocalization in XFEL-heated Fe_3O_4

Figure 4.1: Operation of an x-ray free electron laser (cite McNeil). Electrons enter the undulator with random phases and originally emit uncoherent radiation at the undulator's resonant wavelength. As the electrons propagate, random fluctuations in the radiation field causes them to bunch at the resonant wavelength and emit coherently.

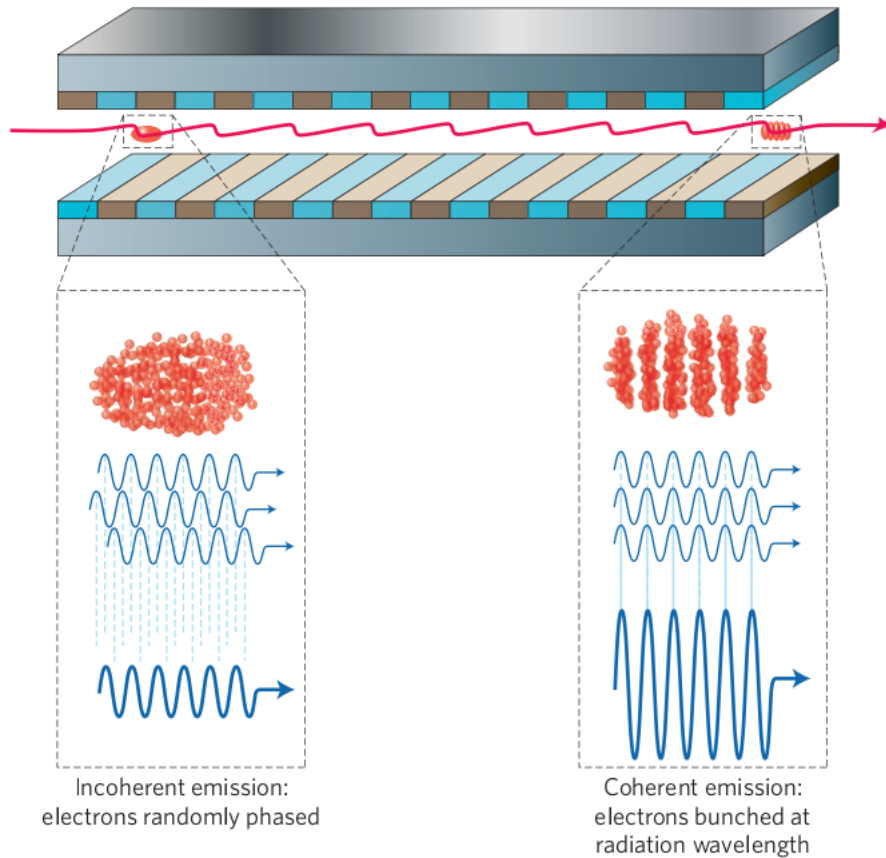


Figure 4.2: Schmematic representation of a two-color XFEL x-ray diffraction measurement wherein a chemical filter is used to reject pump photons.

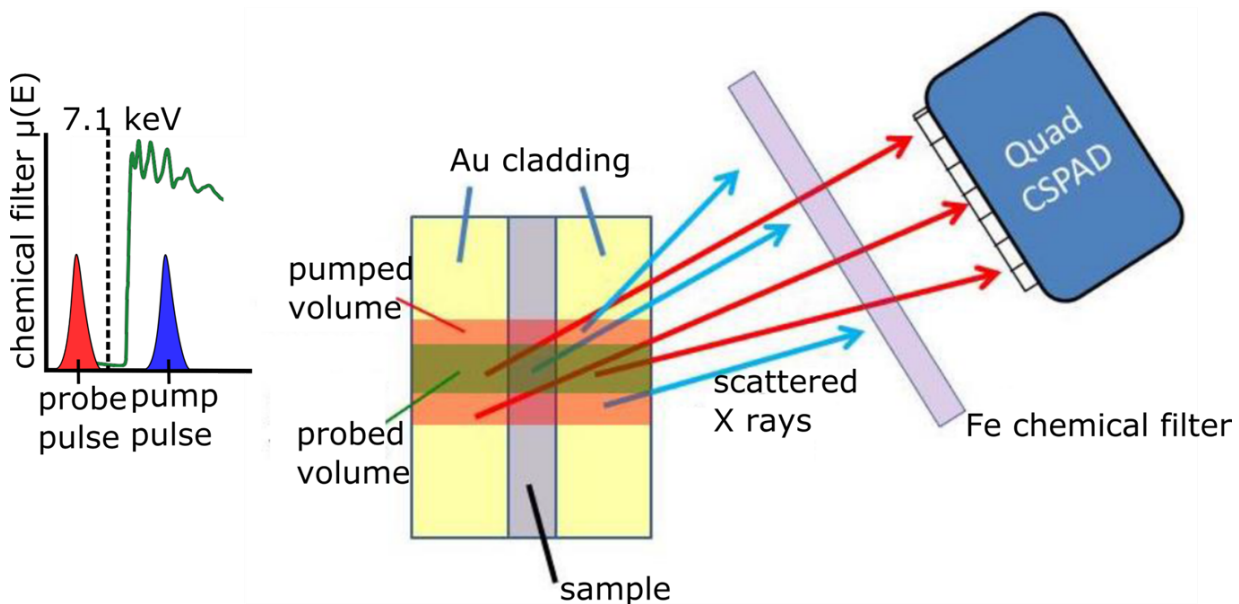


Figure 4.3: Left: intensity of diffraction peaks as a function of temperature, using finite-temperature DFT calculations in VASP; right: intensity of diffraction peaks as a function of ionization, using an atomic form factor-based model of ionization. The four simulated compounds are (from top to bottom) LiF, diamond, graphite, and Be. Taken from Valenza et al. (cite Valenza et al.)

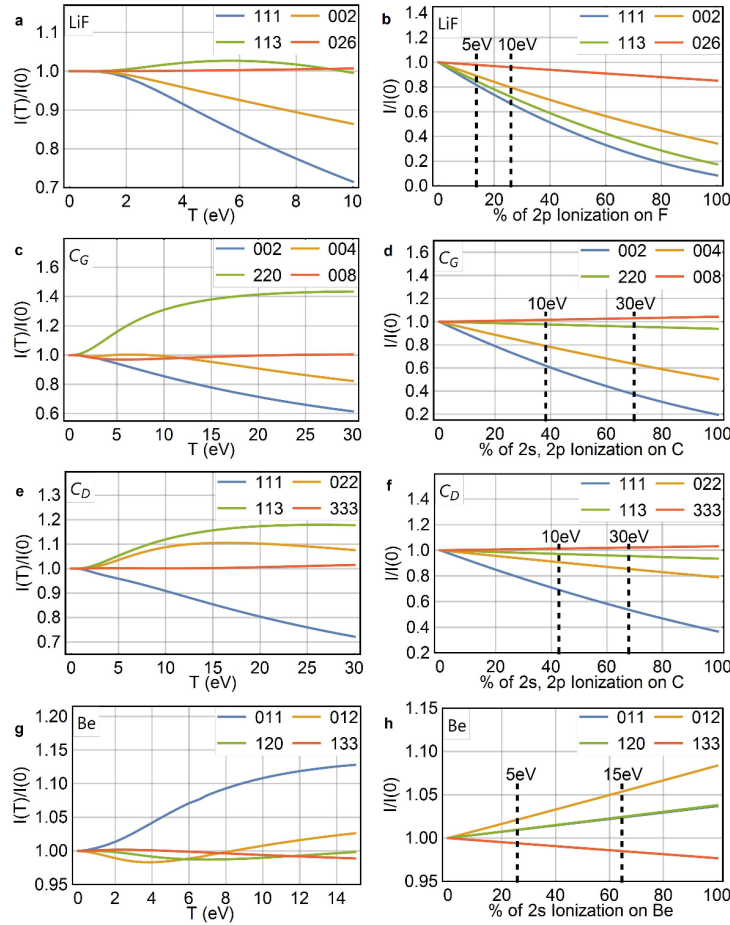


Figure 4.4: Progression of Bragg peak intensities as a function of incident x-ray flux density for (a) microphase and (b) nanophase Fe_3O_4 , normalized to the intensity of the lowest-flux density point. (c) displays the progression of Bragg peak intensities as a function of electron ionization in an atomic form-factor based model wherein the Fe 3d and O2p electrons are first ionized, followed by the more tightly-bound Fe 4s and 3p, and O 2s electrons. (cite Fe_3O_4 paper in preparation)

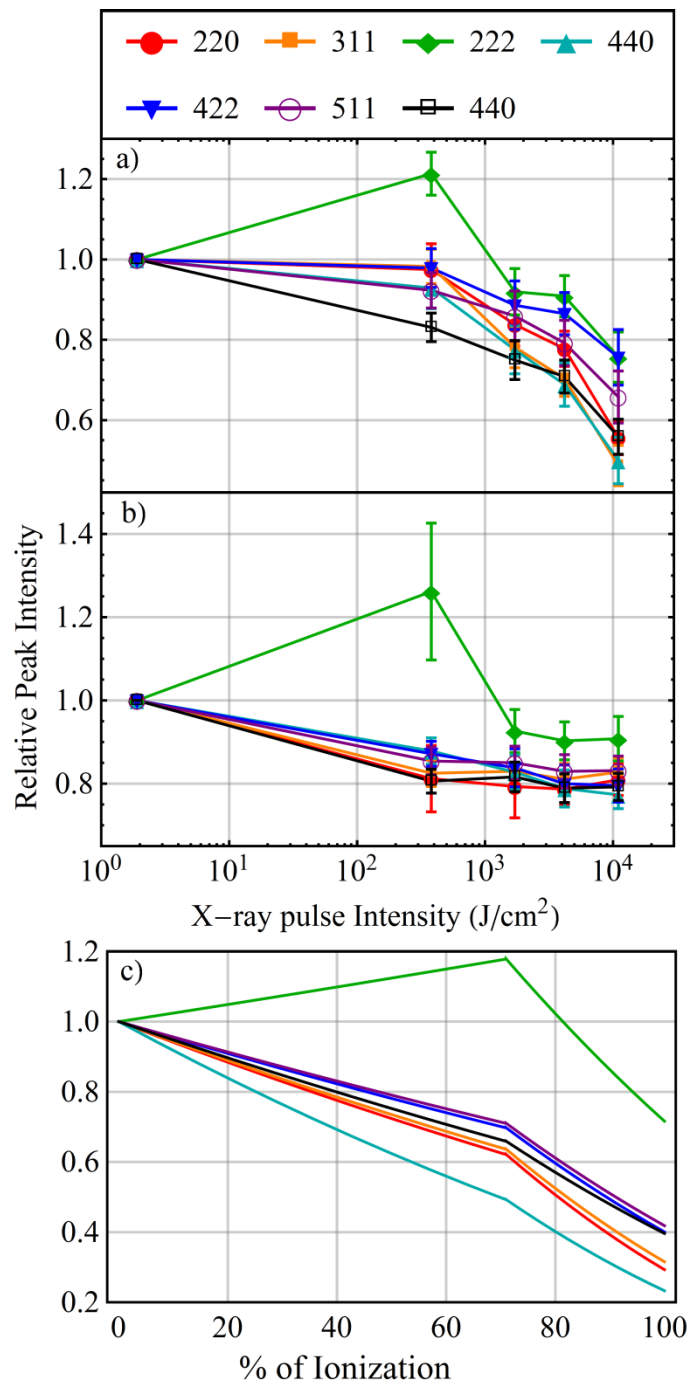


Figure 4.5: Same data as Fig. 4.4 plotted against Bragg angle and compared with the Debye-Waller factor for several values of RMS atomic displacement. (cite fe3o4 paper in preparation)

